FLOW AND ENTRAINMENT MECHANISMS AROUND A FRESHWATER MUSSEL ALIGNED WITH THE INCOMING FLOW

Hao Wu[1], George Constantinescu[1] and Jie Zeng[2]

[1]Department of Civil and Environmental Engineering and IIHR-Hydroscience and Engineering, The University of Iowa, Iowa, USA

[2]South Florida Water Management District, West Palm Beach, Florida, USA

ABSTRACT

The paper uses information from eddy-resolving simulations to characterize flow and turbulence around freshwater mussels at the organism scale. The focus is on the simplest case of a partially burrowed, isolated mussel aligned with the incoming flow in an open channel. The wake structure and the capacity of the flow to displace the mussel from the bed substrate and to induce local scour around the mussel are investigated as a function of the ratio between the height of the exposed part of the mussel, h, and the total mussel height, d, and as a function of the filtration velocity ratio (VR) between the incoming channel flow velocity, U_0, and the mean velocity inside the excurrent siphon, U_e. As opposed to flow past most surface-mounted obstacles where the bed shear stresses are reduced in the wake of the body, the capacity of the flow to induce bed erosion behind isolated mussels aligned with the flow is relatively large because of strong downwelling motions inside the horizontal separated shear layers. These flow features are associated with the formation of counter-rotating base vortices of unequal coherence that induce upwash behind the mussel. The total circulation of the base vortices increases with increasing h/d and VR. Though both symmetrical and anti-symmetrical shedding are observed in the wake, the anti-symmetrical mode dominates and its strength increases with increasing VR. The nondimensional streamwise force acting on the emerged part of the mussel's shell increases with increasing h/d and VR. Finally, the paper discusses the effects of varying h/d and VR on the dynamics and dilution of the jet of filtered water originating in the excurrent siphon, which is important to understand how mussels affect mixing and water quality (e.g., nutrient availability, phytoplankton concentration) in natural streams.

Keywords: freshwater mussels, turbulence, active filtering, numerical simulations

1. INTRODUCTION

Freshwater mussels are bivalve mollusks that live at the sediment-water interface in sand-bed and gravel-bed rivers and can actively adapt to the surrounding environment. Their shell contains two valves that are close to symmetric. The shell is partially burrowed in the substrate of the river channel (Fig. 1a). Using their foot, mussels can slowly migrate and change their orientation. They can modify their filtering flow rate and increase or decrease their degree of body exposure to the flow such that they are not displaced from the substrate in which they are anchored during flood events. To increase their stability, mussels tend to orient themselves

parallel to the incoming flow. Mussels also contain two siphons on their posterior side. Water containing particulate organic material, nutrients, phytoplankton, zooplankton and dissolved organic matter enters the mussel through the incurrent (inhalant) siphon. Filtered water depleted of nutrients, fine suspended matter and waste leaves the mussel through the excurrent siphon (Vaughn et al., 2004, 2008). As a result, freshwater mussels act as ecosystem engineers and are a main contributor to purifying the water in natural streams. Moreover, mussels help stabilizing the bed surface, provide habitat/refuge for benthic organisms, redistribute nutrients and increase the dissolved oxygen concentration in the soil substrate (Lohrer et al., 2004; Allen and Vaughn, 2009). Mussel excretion can account for a large part of the nitrogen available in the river food web (Atkinson et al., 2014). Freshwater mussels are also good indicators of water quality in rivers based on the levels of toxic substances and pollutants accumulated in their tissue.

As mussels generally live for tens of years, they need to be able to withstand extreme flow conditions such as large floods. During such events, bed scour and drag forces acting on the mussels are larger, which can lead to their displacement from the substrate in which they are anchored. Moreover, loss of habitat, dam construction, harvesting and the presence of invasive mussel species have led to a decline in mussel populations in many rivers (Strayer et al., 2004; Haag, 2012). As a result, many species of freshwater mussels are now listed as imperiled. Improving habitat conditions for imperiled freshwater mussels can stop the decline and restore freshwater mussel communities in rivers (Nakato et al., 2007). It is generally agreed that habitat suitability is a function not only of substrate characteristics but also of hydrodynamic conditions, as these conditions control the stability of the river bed and the capacity of the mussels to remain anchored into the bed substrate (Englehardt et al., 2004). Hydrodynamics also affects turbulent entrainment of nutrients into the benthic boundary layer where nutrients are depleted due to consumption. Unfortunately, little is known on how freshwater mussels interact with their hydrodynamic habitat both at organism scale and at river reach scale where mussels generally live in large colonies (Howard and Cuffey, 2003). For sufficiently high densities of the mussels forming the colony, the hydrodynamic conditions and the availability of nutrients, phytoplankton and other transported matter around a particular mussel are a strong function of the relative position of the mussel inside the mussel bed and the proximity of other mussels.

The present numerical study focuses on investigating flow and turbulence structure surrounding isolated, partially-burrowed mussels, drag forces acting on the exposed part of the mussel's shell and sediment entrainment mechanisms that lead to local scour and, eventually, to displacement of the mussel from the bed. Though, as already mentioned, mussels generally live in colonies, small clusters or even isolated mussels can be observed in rivers. Flow conditions near the most upstream mussels of a mussel bed are also close to those observed around isolated mussels. The case of an isolated mussel also serves as a limiting case with respect to which one can quantify changes in flow conditions due to mussel-to-mussel interactions that become more important with increasing density of the organisms forming the mussel bed.

The turbulent flow past the exposed part of the mussel's shell is highly three-dimensional and induces the formation of energetic coherent structures that play an important role in bed erosion, particulate and nutrient transport. Active filtering by the mussel is also thought to affect not only the mean flow and turbulence around the posterior side of the mussel but possibly the drag forces acting on the mussel's shell and transport of matter and particulates. The present study focuses on the case where the major axis of the mussel is oriented parallel to the incoming flow direction, which is the orientation that results in minimum streamwise drag force acting on the exposed part of the mussel's shell. A main goal of the present study is to elucidate near-bed flow hydrodynamics past partially burrowed mussels with and without filter feeding. To address this goal, we conduct a parametric study in which we vary the filtering velocity ratio (VR) and the degree of shell exposure.

2. REVIEW OF EXPERIMENTAL AND NUMERICAL INVESTIGATIONS

Several relevant experimental studies were conducted to investigate the hydrodynamics of flow past wall-mounted, submerged, idealized-shape obstacles (e.g., Okajima, 1982; Savory and Toy, 1986, 1988; Okamoto and Uemura, 1991; Okamoto and Sunabashiri, 1992; Shamloo et al., 2001; Martinuzzi and AbuOmar, 2003; Sumner et al., 2004; Pattenden et al., 2005; Hajimirzaie et al., 2012; Hajimirzaie and Buchholz, 2013). In particular, the eddies generated around fully submerged, low-aspect-ratio obstacles (e.g., streamline and transverse oriented semi-ellipsoids, vertical cylinders and hemispheres) and the wake structure of these obstacles bear important similarities with those observed for isolated, partially burrowed mussels. Besides the horseshoe vortices in front of the obstacle, vortex tubes are present in the separated shear layers (SSLs). The shape of the vortex tubes corresponds to that of the detachment line/lines on the body. For noncircular obstacles, these studies have also shown that the coherence of the various vortices and the dominant shedding frequency in the wake are a function of the orientation of the obstacle relative to the incoming flow direction. Generally, an increase in the angle of attack increases the degree of bluntness of the obstacle and generates stronger vortices both in front and in the wake of the obstacle. Shamloo et al. (2001) found that the deformations of the free surface are negligible if the relative submergence (e.g., the ratio between the flow depth, D, and the height of the emerged obstacle, h) is larger than four.

Several experimental investigations were conducted in laboratory flumes with partially burrowed mussels. They included live mussel experiments (e.g., see Butmann et al., 1994; Sansom et al., 2018; Kumar et al., 2019). If the mussel is aligned with the flow, the mussel's shell resembles a fairly streamlined, but slightly asymmetric body. The filtering flow through the two siphons can disturb the formation of coherent structures generated in the SSLs. Motivated by the fact that some field observations showed no particular orientation of the siphons relative to the flow direction, while others showed that siphons are generally pointed upstream (Di Maio and Corkum, 1997), Kumar et al. (2019) performed experiments for isolated live mussels oriented parallel to the flow with siphons facing both upstream and downstream. Some flume studies of flow past a mussel bed included the siphonal flows but were conducted with very idealized shapes of the mussels (e.g., Crimaldi et al., 2007). Other experimental studies used dead mussels or realistic models of dead mussels (e.g., Crimaldi et al., 2002;

Constantinescu et al., 2013) but did not account for the siphonal flows. In a recent study, Sansom et al. (2018) added a pair of flexible PVC tubes inside a dead mussel shell through which water was pumped at a constant rate to account for the siphonal flows and used 2-D particle image velocimetry (PIV) to measure the velocity field and turbulent kinetic energy in selected planes for a half-burrowed mussel placed in a flume with a gravel-bed.

Numerical studies can also help understanding flow and transport processes around freshwater mussels provided that they can capture the large-scale coherent structures in the flow. This requires the use of large eddy simulation (LES) techniques that directly resolve the energetically important eddies in the flow. Compared to laboratory studies that generally provide information in a limited number of 2-D sections, eddy-resolving simulations provide 3-D information on the flow and coherent structures, allow estimating the bed shear stresses and the drag forces acting on the mussels. Such an LES study was reported by Constantinescu et al. (2013) who investigated flow past a cluster of three non-filtering, half-burrowed freshwater mussels placed at an angle of attack of 90^0 with respect to the incoming flow direction. The present study adopts a similar numerical approach but focuses on an isolated freshwater mussel (*Lampsilis siliquoidea*) placed at an angle of attack of 0^0 in a flat-bed open channel with fully developed, turbulent incoming flow.

3. NUMERICAL MODEL

3.1 Viscous flow solver and turbulence model

The finite-volume, non-hydrostatic, 3-D flow solver in the commercial code STAR-CCM+ (CD-Adapco) was employed to perform the numerical simulations. A hybrid approach called Detached Eddy Simulation (DES) was used to resolve the energetically important eddies in the flow. DES reduces to unsteady RANS near the solid boundaries and to LES in the rest of the computational domain (Spalart 2000; Chang et al., 2007). Use of LES and hybrid RANS-LES methods like DES was shown to result in more accurate predictions of the mean flow and turbulence statistics for complex turbulent flows such as flow in natural channels, flow past surface-mounted obstructions and flow over rough surfaces (Constantinescu and Squires, 2003; Constantinescu et al., 2003; Keylock et al., 2005, 2012). For such flows, DES that resolves the viscous sublayer was shown to be of comparable accuracy to LES without wall functions, but computationally much less expensive (Rodi et al., 2013).

The present simulations were conducted with the Spalart-Allmaras, 1-equation model as the base RANS model (Spalart and Allmaras, 1992). A transport equation was solved for the modified eddy viscosity, $\tilde{v}$. Away from the solid boundaries, the definition of the length scale in the destruction term of the transport equation solved for $\tilde{v}$ is modified such that the eddy viscosity becomes proportional to the grid size, like in classical LES. The governing equations are integrated through the viscous sublayer and no wall functions are used. The IDDES version of DES was used to perform the simulations discussed in the paper (Rodi et al., 2013). This advanced version of DES eliminates or reduces some of the problems reported with the standard version of DES such

as premature switch to LES mode and the log-layer mismatch between the regions where the RANS and LES modes are active in attached-boundary-layer flows. The use of resolved turbulence in the flow fields specified at the channel inlet further alleviates these problems (Koken et al., 2013; Zeng et al., 2008). The full model DES equations and coefficients can be found in Spalart (2000) and Rodi et al. (2013).

The governing equations are discretized and solved on unstructured, Cartesian-like grids. The code allows using nested Cartesian grids with cell cutting near boundaries of complex shape. The viscous flow solver employs the SIMPLE (Semi-Implicit Method for Pressure Linked Equations) algorithm to achieve pressure-velocity coupling for the discretized Navier-Stokes equations. In the SIMPLE algorithm, an intermediate velocity is obtained by solving the momentum equations without the pressure gradient term. The intermediate velocity field does not satisfy the continuity equation. A pressure correction algorithm is used to modify the pressure field such that the final velocity field satisfies continuity. The convection terms in the momentum equations are discretized using the 3rd order MUSCL scheme to keep numerical dissipation low. The convective terms in the transport equations solved for the modified eddy viscosity and the passive scalar introduced in the excurrent siphon are discretized using the second-order-accurate upwind scheme. The diffusive and pressure gradient terms are discretised using the second-order-accurate, central scheme. The implicit temporal discretization is second-order accurate. The viscous solver in STARCCM+ is parallelized using MPI. The same solver was previously used to conduct unsteady RANS and DES simulations in our group for complex turbulent flows. These studies (e.g., Wu et al., 2020; Horna-Munoz and Constantinescu, 2018, 2020; Cheng et al., 2018) also include detailed validation with experimental data.

3.2 Simulations set up

To define the boundaries of the computational domain and generate the mesh, the most critical part is obtaining a detailed mapping of the mussel's shell geometry (Fig. 1). A stereo lithography (STL) file containing the geometry of the two valves was provided by the team at the SUNY Univ. at Buffalo who used 3-D tomography to map the external surfaces of a mussel (Lampsilis siliquidea) used in their laboratory experiments (Sansom et al., 2018). Once read in AUTOCAD, the geometry was cleaned of its spurious parts. Then, the geometry of the two valves was assembled into one surface and the boundary surfaces corresponding to the two siphons were defined. The computational domain contains the posterior end of a mussel in a partially burrowed state (Fig. 1b). Except for one simulation, the mussel was oriented parallel to the streamwise direction with the siphons pointing upstream. The angle of attack for these cases was defined as being $\theta=0^0$ (Table 1). One simulation was performed with the siphons pointing downstream, which formally corresponds to $\theta=180^0$. The burrowed part of the mussel was eliminated and a short, straight, vertical pipe connecting to the excurrent siphon was added in the simulations with VR>0. This allows the excurrent jet flow (Riisgård et al., 2011) to develop in a more realistic way around the region where the flow through the excurrent siphon enters the channel. No pipe was added in the VR=0 simulations where the surfaces corresponding to the two siphons were treated as no-slip surfaces.

The mesh generator in STAR-CCM+ allows the use of various controls and the generation of fine meshes in different parts of the domain where the flow resolution needs to be higher. First, the surface mesh on the boundaries of the computational domain is generated (Fig. 1c). Hexahedral meshes are created based on the specified cell size on the boundary surface. Automatic grid refinement is then applied in regions containing surfaces of complex shape. Trimmed cells are added near these surfaces. This procedure also ensures a smooth transition to regions where the mesh is coarser. The prism layer meshing function in STARCCM+ was used near solid boundaries to refine the mesh close to the mussel's surface such that the first point off this surface is situated inside the viscous sublayer.

Table 1 Main flow and geometrical parameters and predicted variables for the simulated cases (θ is the angle of attack, U_0 is the incoming channel flow velocity, U_e is the mean exit velocity in the excurrent siphon, $VR=U_e/U_o$, h is the height of the exposed part of the mussel, d is the total mussel height, b is the maximum width of the mussel at the channel bed, AR=h/b, D is the channel flow depth, Q_e is the volumetric discharge in the excurrent siphon, $Re_b=bU_0/\nu$, $Re_h=hU_0/\nu$, ν is the molecular viscosity, x_r is the length of the bubble containing flow moving upstream at the back of the mussel measured from the center of the mussel (x=0), $St_H=f_Hb/U_0$, f_H is the frequency of the full oscillatory cycle of the horseshoe vortex system, $St_W=f_Wb/U_0$, f_W is the dominant anti-symmetric wake shedding frequency).

θ (^{o})	VR (-)	h/d (-)	AR (-)	D/h (-)	U_0 (m/s)	Q_e $\times10^6$ (m^3/s)	Re_b $\times10^4$ (-)	Re_h $\times10^4$ (-)	x_r/d (-)	x_r/h (-)	St_H (-)	St_W (-)
0	0.13	0.5	0.75	5.0	0.3	1.66	1.3	1.0	0.95	1.9	0.19	0.37
0	0.13	0.375	0.64	6.7	0.3	1.66	1.2	0.8	0.90	2.4	-	0.35
0	0.13	0.25	0.50	10.0	0.3	1.66	1.0	0.5	0.75	3.0	-	0.34
0	0	0.5	0.75	5.0	0.3	0	1.3	1.0	1.0	2.0	0.19	0.32
0	0.5	0.5	0.75	5.0	0.3	6.38	1.3	1.0	0.90	1.8	0.19	0.38
0	0.7	0.5	0.75	5.0	0.3	8.94	1.3	1.0	0.85	1.7	0.19	0.39
0	0.05	0.5	0.75	5.0	0.75	1.66	3.4	2.5	0.95	1.9	0.19	0.40
180	0.7	0.5	0.75	5.0	0.3	8.94	1.3	1.0	0.60	1.2	0.26	0.20

The flow depth was D = 0.15 m. The other dimensions of the computational domain were L=0.4 m (L/D=2.66) and B=0.4 m (Fig. 1b). The length scale used in the simulations was d=0.06 m, which corresponds to the total height of the mussel (Fig. 1a). Most of the simulations (Table 1) were conducted with an incoming channel flow velocity, U_0=0.3 m/s, which corresponds to the value used in the validation experiment of Sansom (2019). One simulation was conducted with a higher velocity value, U_0=0.75 m/s.

The volumetric discharges through the incurrent (Q_i) and excurrent siphons (Q_e) were equal. The range considered in the simulations was $0 \leq Q_e \leq 8.94\times10^{-6}$ m^3/s (Table 1). This corresponded to a filtration velocity

ratio, VR=U_e/U_o, between 0 and 0.7. Most of the simulations were conducted with $Q_e=1.66\times10^{-6}$ m^3/s, which corresponds to an excurrent siphon velocity U_e=0.05 m/s. The peak value of Q_e corresponds to U_e=0.27 cm/s, which is slightly above the maximum excurrent siphon velocity reported by Sansom et al. (2018) in their live mussel experiments and close to the maximum volumetric flow discharge in unionids reported by Price and Schiebe (1978). Simulations were conducted with three different levels of mussel burrowing for which h=0.5d, 0.375d and 0.25d (Fig. 1c). For the highest degree of exposure of the mussel, (h/d=0.5), the maximum length and width of the partially-burrowed mussel were l/d≈1 and b/d=0.65, respectively, giving l/b≈1.5 and an aspect ratio AR=h/b≈0.75. The Reynolds number calculated with U_0 and the width of the exposed part of the mussel was Re_b≈13,000 (Table 1).

The channel bed and the emerged part of the mussel's shell were treated as no-slip smooth surfaces. The free surface was treated as a zero-shear-stress boundary. This is an acceptable approximation given the low value of the channel Froude number (<0.3). The mean velocity was specified at the inlet of the pipe through which the excurrent siphon flow was advected into the channel. The outflow discharge was specified on the surface corresponding to the incurrent siphon. The lateral surfaces were treated as symmetry boundaries on which the normal velocity component was equal to zero. This type of boundary conditions is more appropriate for the case one is interested to study flow past an isolated mussel situated away from any boundaries (e.g., channel banks). Precursor simulations of fully-developed, turbulent flow in a straight periodic channel of depth D and width B were conducted with the corresponding value of U_0. The instantaneous flow fields in a cross section were saved over $30D/U_0$ at a time interval of $0.01D/U_0$ and then fed in a time-accurate way in the simulations conducted for flow past an isolated mussel. Linear interpolation in time was used in between consecutive fields. The predicted mean nondimensional streamwise velocity profile at $Re_D=U_0D/\nu$ was in agreement with data collected at comparable Reynolds numbers for smooth-bed channels. The nondimensional bed friction velocity was close to the value expected for a fully-developed flow (e.g., $u_{\tau0}/U_0$≈0.047 for Re_D=45,000). A convective boundary condition was used at the exit section. The concentration of the scalar, C, was set to zero at the inlet of the domain and to C_0 at the inlet of the pipe connected to the excurrent siphon. Second order extrapolation was used to estimate C at the outlet boundaries. A zero gradient condition was imposed for C at the other boundaries.

Preliminary simulations were conducted to ensure that the width and length of the computational domain used in the simulations reported in the paper were sufficiently large for the mean flow and turbulence statistics to be independent of the domain size. The grids were refined near all solid surfaces. The level of mesh refinement in the wall normal direction was such that the viscous sublayer contained two grid points. The mesh was refined around the shell to resolve the horseshoe vortex and the vortex tubes inside the SSL. Simulations with different levels of grid refinement were conducted for some of the h/d=0.5, U_0=0.3 m/s cases. The minimum number of grid cells needed to get grid independent solutions in the aforementioned computational domain was slightly larger than one million. However, simulations are reported on grids containing close to 2 million cells. For these

grids, the average cell size in the directions parallel to the shell's surface was about 20 wall units close to the mussel.

3.3 Validation

Several validation simulations were performed for flow past an isolated mussel with $\theta=0^0$ using the experimental data collected by SUNY Univ. at Buffalo (Sansom, 2019). The experiment was performed in a recirculating hydraulic flume that was 10.7 m long and 0.5 m wide (Sansom et al. 2018). The streamwise velocity profile was measured at the center of the flume, 0.5 m upstream of the mussel's location using an Acoustic Doppler Velocimeter (ADV) Vectrino Profiler and a two-dimensional Particle Image Velocimetry (PIV) system was used to collect data in several planes. Details of the flume and instrumentation used for data collection are given in Sansom et al. (2018) who performed similar gravel-bed experiments of flow over an isolated mussel and a large cluster of mussels in the same flume. For the validation experiment (Sansom 2019), the bed was smooth, the flow depth was $D\approx0.15$ m, the mean incoming velocity was $U_0=0.3$ m/s and only one model mussel with $h/d=0.5$, $b/d=0.65$ and $Q_e=0$ (VR=0) was introduced in the flume. The model mussel was constructed from oak wooden blocks designed using a 3-D scan of a *Lampsilis siliquoidea* shell.

Table 2 Inlet mean velocity profile, U/U_0 vs. z/D, in the validation experiment and simulations

z/D	U/U_0
0.07	0.808
0.2	0.884
0.33	0.910
0.47	0.997
0.6	1.025
0.73	1.071
0.87	1.120

To better mimic the experimental conditions, the computational domain used in the validation simulation was 0.5 m wide, the lateral boundaries were treated as no-slip walls, the mesh was refined near the lateral walls to resolve the attached boundary layers and the inlet section that was situated 0.5 m upstream of the mussel where the mean velocity streamwise profile was measured (Table 2). Though the boundary layer extended up to the free surface, the measured mean velocity profile showed some differences with the standard fully-developed, turbulent open channel flow profile in a wide open channel. Simulations were performed on a coarser mesh with about 1.5 million cells and on a finer mesh with about 4 million cells. The simulations matched the measured streamwise velocity profile at the inlet section of the computational domain but had to approximate the inflow turbulence characteristics due to lack of detailed information.

Figure 2 compares the nondimensional mean streamwise velocity (U/U_0) and turbulent kinetic energy (TKE/U_0^2) profiles measured in a horizontal plane (z/h=0.5) cutting at about mid distance between the channel bed (z=0

m) and the top of the exposed part of the mussel (z=0.03 m). The profile at x/b=1.28 cuts through the horizontal SSLs, which explains the two peaks of the TKE around y/b=-0.45 and y/b=0.45. The profile at x/b=2.56 cuts through the near-wake region. Overall, the differences between the streamwise velocity and turbulent kinetic energy profiles predicted by the two simulations are sufficiently small to conclude that the solutions are grid independent. Moreover, the predicted streamwise drag force acting on the mussel and the dominant wake shedding frequencies differed by less than 2% between the two simulations. Some larger differences are observed between the numerical predictions and the experimental data in Fig. 2. They are most probably due to differences in the mean flow (e.g., due to secondary currents forming in the flume) and turbulence characteristics at the location of the inlet cross section. The wake flow seems to recover faster in the simulation compared to the experiment, which triggers the underprediction of the velocity deficit inside the wake (see velocity profile at x/b=2.56 in Fig. 2b. The TKE predictions at the same streamwise locations are in fairly good agreement with the experimental data.

4. WAKE REGION

4.1 Dynamics of the vortex tubes and separated shear layer

Figure 3a visualizes the vortical structures in the instantaneous flow for the $\theta=0^0$, VR=0, h/d=0.5 case. It shows that U-shaped vortex tubes are shed away from the separation line on the mussel's shell. These vortex tubes are severely stretched via interaction among neighboring tubes or with energetic eddies that are present inside the recirculation region at the back of the mussel. At most time instances, the heads of the U-shaped tubes are tilted toward the downstream direction (Fig. 3a), though vortex tubes that move with little disturbance of their heads or that slightly tilt toward the back of the mussel are also observed at times. Given that there is no active filtering for this case, results can be qualitatively compared with those obtained for semi-ellipsoids by Hajimirzaie and Buchholz (2013). Based on analysis of the correlations of the instantaneous velocity, they concluded that vortex tubes tilt upstream for a semi-ellipsoid with AR=0.89 and downstream for a semi-ellipsoid with AR=0.67. They related this change in the dynamics of the vortex tubes to the presence of upwash or downwash induced by tip or base vortices forming at the back of the semi-ellipsoid. For the VR=0, h/d=0.5 case, the aspect ratio is AR=0.75 and downstream tilting dominates. This result is consistent with the model proposed by Mason and Morton (1987) that associates upwash induced by base vortices with downstream tilting of the vortex tubes near the obstacle.

Regardless of the tilting direction of the vortex tubes close to the mussel, the head of each vortex tube is advected faster than its legs at distances larger than two times the body width from the back of the mussel. The head is situated in a region of larger mean streamwise velocity compared to the base part (legs) of the vortex tube. This induces severe stretching of the legs of the U-shaped tubes that move from being vertical to making a small angle with the bed (e.g., see the most downstream hairpin in Fig. 3c). As a result, most of the vortex tubes in the near wake resemble large-scale hairpins. The dimensions of these hairpins scale with the height of the exposed part of the shell, h.

As mussel filtering becomes active (VR>0), the excurrent jet strongly disturbs the part of the SSL situated on top of it. The tops (heads) of the vortex tubes are strongly disturbed by the jet, which may cause these tubes to break into two separate eddies. The effects of the excurrent jet on the SSL can be better understood by comparing the instantaneous spanwise vorticity distributions in the y/d=0 plane shown in Fig. 4. The main effect of increasing VR is to augment the angle between the SSL and the horizontal. The vorticity levels inside the eddies present near the back of the mussel are also increasing, which has a direct effect on the TKE in this region. Besides disturbing the vortex tubes, the interaction of the jet with the incoming flow that tries to accelerate the jet in the streamwise direction generates large-scale hairpins for sufficiently large VR values. The jet shear layer is severely skewed and jet shear layer vortices are generated on the upstream side of the jet (Mahesh, 2013). Such hairpin vortices are present in the VR=0.7, h/d=0.5 simulation (Fig. 3b). They are qualitatively similar to those observed by Sau and Mahesh (2008) for a round jet in crossflow with VR=1. These hairpins disturb the vortex tubes and decrease the regularity of the interactions between the two legs of same vortex tube which results in a weakening of the symmetric wake shedding mode (see section 4.5).

4.2 Flow structure behind the mussel

The 2-D streamline patterns in Fig. 5 show the presence of a recirculation eddy just beneath the SSL in the y/d=0 plane for the h/d=0.5 simulations with VR≤0.5. This eddy corresponds to a cut through the top of an arch vortex forming at the back of submerged surface-mounted obstacles (e.g., see Pattenden et al., 2002; Chang and Constantinescu, 2020). The two recirculation bubbles present at the back of the mussel in Fig. 7b correspond to the legs of the arch vortex. For constant U_0 and h/d, the size of the arch vortex decreases with increasing VR such that the vortex is not present in the VR=0.7 simulation despite the fact that two recirculation bubbles are still forming at the back of the mussel in horizontal planes situated close to the bed. The size of the U-shape vortex decreases with increasing U_0 for constant Q_e and h/d. The vortex does not form in the simulations with h/d ≤0.375. In the h/d=0.5 simulations, a second recirculation bubble is present in the y/d=0 plane. For low VR values, this eddy is situated close to the junction between the back of the mussel and the channel bed. As VR increases, this bubble starts moving away from the channel bed.

The region containing one or two recirculation bubbles or the one in which the mean flow moves toward the back of the mussel if no recirculation bubbles form is defined as the recirculation flow region. Its length, x_r, is measured with respect to the middle of the mussel, which approximatively corresponds to the point on the shell with the highest elevation with respect to the bed, h (see VR=0.13, h/d=0.5 case in Fig. 5). For flow past regular obstacles (e.g., submerged cylinders, ellipsoids, pyramids), it is customary to report x_r/h, where x_r corresponds to the reattachment length of the recirculation bubble at the channel bed. Our definition is different given that the width of the region where the flow recirculates is not always the largest at the channel bed. Figure 6a shows that for constant h/d and U_0, x_r/h decreases close to linearly with increasing VR. Increasing U_0, while keeping constant Q_e and h/d, has a negligible effect on x_r. Reversing the incoming flow, while keeping all the other flow

and geometrical parameters unchanged, decreases x_r by about 25%. For constant U_0 and VR, x_r/h increases close to linearly with decreasing h/d (Fig. 6b). However, x_r increases monotonically with increasing h/d (Table 1).

As for submerged, surface-mounted obstacles of regular shape, the TKE is strongly amplified at the end of the SSL where the legs of the vortex tubes start interacting to shed wake vortices (Fig. 7b). In the vertical direction (Fig. 7a), the region of high TKE is also bounded by the SSL. The length of the region of high TKE (TKE/U_0^2>0.08) at the back of the mussel scales with h and its width scales with the mussel width, b (Fig. 1c). In the vertical y/d=0 plane, the region of high TKE at the back of the mussel contains two subregions of high TKE. These subregions are even better delimited in Fig. 5 showing the pressure rms fluctuations, $p_{rms}/\rho U_0^2$. The top subregion of high flow turbulence is mostly due to the passage of the vortex tubes inside the SSL (Fig. 4), while the bottom one is situated just downstream of the second recirculation eddy (Fig. 5). For constant h/d and U_0, the effect of increasing VR is to decrease the streamwise length of the region of high TKE and, at the same time, to increase the peak TKE/U_0^2 and $p_{rms}/\rho U_0^2$ levels inside this region (Figs. 5 and 7a).

4.3 Streamwise-oriented vortices

A common feature of the present cases with streamwise-oriented, partially burrowed mussels (AR≤0.75) is the formation of a pair of counter-rotating base vortices that advect fluid upwards in between their cores (upwash flow). These vortices as visualized in Fig. 8 and in the x/d=0.55 planes in Fig. 9. For high relative submergence, Hajimirzaie et al. (2012) reported the formation of tip counter-rotating vortices that advect fluid downwards in between their cores (downwash flow) in the wake of streamwise-oriented (major axis parallel to the incoming flow) semi-ellipsoids with AR=0.89 and of base counter-rotating vortices in the wake of spanwise-oriented ellipsoids with AR=0.67. It is not clear if the formation of base vortices rather than tip vortices for the flow and mussel geometry considered in the present study is due to the particular shape of the mussel or to the relatively low aspect ratio of the emerged part of the shell (AR≤0.75) compared to the ellipsoid (AR=0.89) for which downwash was reported by Hajimirzaie et al. (2012).

As opposed to the case of symmetrical obstacles of regular shape, the coherence of the two vortices is generally very different away from the mussel's back (x/d≥1 planes in Fig. 9). Due to the asymmetry of the shell, the left vortex is more coherent (e.g., higher circulation) than the right vortex in the $\theta=0^0$ simulations. The opposite is true in the $\theta=180^0$ simulation. Reducing the emerged height of the mussel generates counter-rotating vortices of more comparable coherence (e.g., see Figs. 8 and 9 for the VR=0.13, h/d=0.25 case where the Q criterion shows the presence of two streamwise oriented vortices at the back of the mussel). In cases with larger h/d, the vortex on the right side is observed only very close to the mussel, which explains why the Q criterion shows the presence of only one vortex for the VR=0.7, h/d=0.5 case in Fig. 8. The coherence of the stronger vortex increases monotonically with increasing VR (e.g., compare Figs. 9b and 9c).

The pair of base vortices is observed in all simulations in the x/d=0.55 section except for the h/d=0.5, VR=0.7 case (Fig. 9c) where only one base vortex is observed. These vortices originate close to the bed and their sense of rotation is opposite to that of the co-rotating primary and secondary horseshoe vortices on the same side of the mussel. Away from the bed, the cross flow moves toward the region that corresponds to the back of the mussel (dashed line in Fig. 9). For most cases, the secondary horseshoe vortex loses its coherence for x/d>2 but the primary vortex is still present even at x/d=5. In the h/d=0.25, VR=0.13 case (Fig. 9d) both base vortices can be observed until x/d=2. At larger distances, only the base vortex forming on the left side of the mussel is present and its circulation is comparable with that of the primary horseshoe vortex. In fact, this vortex migrates on the right side of the mussel and starts interacting with the co-rotating leg of the primary vortex. Finally, the vorticity distribution at x/d=0.55 in the h/d=0.5, VR=0.7 case (Fig. 9c) shows the presence of another pair of counter-rotating vortices forming close to the top edge of the mussel. They resemble the vortices that are induced on the leeward side of a classical jet in cross flow with VR>1. Given the low value of VR, they are very weak and are not observed for x/d>1.

As discussed in the next subsection, each base vortex induces flow upwelling on the side of its core where its rotational velocity advects fluid away from the bed and downwelling on its other side. The strength of these upwelling and downwelling motions is proportional to the circulation magnitude of each vortex. Figure 10 shows the total circulation magnitude of the two base vortices as a function of x/d. For constant h/d, the effect of increasing VR on the total circulation magnitude is fairly insignificant until VR≈0.5. For VR≥0.5, the total circulation increases with VR. For constant VR and U_0, the effect of decreasing h/d is to decrease the total circulation of the base vortices.

4.4 Upwelling and downwelling motions in the near wake

Compared to flow past emerged, surface-mounted obstacles, the near-wake flow is much more three dimensional in the case of submerged obstacles. This happens because the incoming flow that is diverted over the top of the obstacle plunges toward the bed as it passes the obstacle. For example, Chang and Constantinescu (2020) observed downwelling inside the SSLs forming on the two sides of submerged cylinders. Upwelling was also observed around the upstream face of the submerged cylinder, near its top boundary. In the case of a partially burrowed mussel oriented parallel to the flow, the upwelling and downwelling motions are stronger and the vertical flow patterns are less symmetric compared to those observed for circular submerged cylinders of same height and width. This is mainly due to the pyramid-like shape of the emerged part of the shell and the asymmetry of the left and right valves. Strong downwelling is observed in the regions surrounding the horizontal SSLs. In most cases, the streamwise extent of the downwelling region on the left side of the mussel and the vertical velocity magnitude inside this region are much larger than those recorded for the downwelling region forming on the right side of the mussel. Another feature observed in most of the simulations is the presence of a region of flow upwelling near the back of the mussel, in between of the two regions of flow downwelling. This flow feature is also qualitatively similar to what was observed for flow past submerged conical bodies and submerged cylinders.

In the case of streamwise-oriented mussels, the relative size of the downwelling regions is controlled by the relative coherence of the two base vortices. For example, the circulations of the two vortices are comparable in the VR=0.13, h/d=0.25 case until x/d=1.5 (Fig. 9b). As a result, the sizes of the downwelling regions forming on the right and left side of the mussel are also comparable (Fig. 11). Figure 9 shows that the base vortex on the left side of the mussel is much more coherent and its coherence increases with increasing VR in the h/d=0.5 cases. Consequently, the length and width of the downwelling region on the left side of the mussel and the vertical velocity magnitude inside this region are increasing monotonically with increasing VR in the h/d=0.5 simulations (Fig. 11). The absence of a counter-rotating base vortex on the right side of the mussel explains the relatively low length of the corresponding downwelling region in the h/d=0.5 simulations. The effect of increasing U_0 for constant h/d and Q_e is to increase the size of the upwelling flow region at the back of the mussel and the vertical velocity magnitude inside the upwelling and downwelling regions (e.g., compare the h/d=0.5, VR=0.05 and VR=0.13 simulations in Fig. 11).

4.5 Wake shedding

Analysis of the instantaneous flow field showed that the anti-symmetric shedding mode is present in all simulations with partially burrowed mussels as the interactions of the horizontal SSLs generate counter-rotating wake billows. However, the wake generated by the mussels did not assume the undulatory shape generally observed for cases with a strong anti-symmetric mode (e.g., for emerged, surface-mounted obstacles). These results are not surprising, as numerical and experimental studies of flow past surface-mounted obstacles of regular shape have shown that shedding is generally present in the wake provided that the height of the obstruction is sufficiently large for the Kelvin-Helmholtz instability to generate vortex tubes in the SSLs. For example, in the case of solid and low-porosity cylinders, Chang and Constantinescu (2020) have shown that the anti-symmetrical shedding mode is strongly damped even for relatively low submergence depths ($D/h<1.33$) compared to the corresponding emerged case ($D/h=1$). Though the wake did not contain the undulations associated with the shedding of counter-rotating billow vortices and pairing between successive vortex tubes took place in the downstream part of the SSLs (symmetric shedding mode), the dominant Strouhal number in the wake, St_w, was still associated with the anti-symmetric shedding mode. However, its energy was much lower (e.g., by about 2 orders of magnitude for $D/h>3$) compared to the emerged case ($D/h=1$).

The presence of counter-rotating base vortices behind the mussel and the associated upwelling in between the horizontal SSLs (Fig. 11) act toward damping the anti-symmetric shedding mode. The mechanism is similar to that observed by Kirkil and Constantinescu (2010) for an emerged cylinder placed on a scoured channel bed. The upflow induced near the symmetry plane by the counter-rotating vortices at the back of the cylinder impedes the SSL from one side to move toward the other side such that vortex tubes from the opposite-side SSL can merge into a wake billow. Besides flow upwelling between the horizontal SSLs, there is another main reason why the weakening of the anti-symmetric mode is expected to be stronger for non-cylindrical obstructions like

457 hemispheres, semi-ellipsoids and partially burrowed mussels. While in the case of cylinders, the vortex tubes
458 generated in the two SSLs are totally independent eddies, in the case of the afore-mentioned, non-cylindrical
459 obstacles, the vortex tubes are U-shaped. Though the two legs of the vortex tube look like independent vortices
460 that are advected inside the horizontal SSLs, they are in fact part of the same vortical structure. Examination of
461 the instantaneous flow fields shows that the interactions between the SSLs on the two sides of the shell involve
462 primarily those between the two counter-rotating legs of the same vortex tube. Even though these legs are
463 deformed and are not situated exactly at the same streamwise position in the region where the horizontal SSLs
464 interact, the symmetric mode is stronger. Finally, the horseshoe vortex system containing highly coherent
465 vortices that follow a quasi-regular cycle, that is symmetric with respect to the horizontal SSLs, also acts toward
466 impeding the lateral anti-symmetrical oscillations of the SSLs (Kirkil and Constantinescu, 2012).
467
468 The instantaneous vertical vorticity distributions in horizontal planes cutting through the mussel in the non-
469 filtering $\theta=0^0$, VR=0, h/d=0.5 case show that though nearly-symmetric interactions between the legs of the same
470 vortex tube occur at times (e.g., see Fig. 12a-b), the dominant interactions are still anti-symmetric (e.g., see
471 Figs. 12c-d). The anti-symmetric interactions generally involve the leg of one vortex tube from one of the
472 horizontal SSLs moving toward the other side such that it interacts not only with the other leg of the same vortex
473 tube but also with the leg of another vortex tube advected inside the horizontal SSL on the opposite side. The
474 most energetic frequency in the wake velocity spectra corresponds to these anti-symmetrical events (St_W=0.32
475 in Fig. 13a and Table 1). The velocity spectra situated not far from the back of the mussel contain a second
476 (less) energetic frequency at St=0.64 (=$2St_w$). This is the nondimensional frequency at which vortex tubes are
477 advected inside the SSL after vortex merging ceases. This finding is consistent with the afore-described anti-
478 symmetric shedding cycle that involves the passage of two vortex tubes. The velocity spectrum in Fig. 13a
479 contains a third energetic frequency. This lower frequency is associated with the symmetric mode $St_s \approx 0.08$
480 (=St_w/4). In this mode, the interactions of the horizontal SSLs are fairly symmetric and result in the shedding of
481 two counterrotating eddies (legs of the same vortex tube) in the near wake (Fig 12a-b). Finally, the presence of
482 more than one energetic frequency in the power spectra was also observed in other investigations of surface-
483 mounted noncylindrical obstacles. For example, Castro et al. (2001) measured spectra containing two energetic
484 frequencies corresponding to a bi-stable shedding regime behind wall-mounted triangular plates.
485
486 The predicted dominant wake frequency for the non-filtering case (St_w=0.32 for D/h=10, AR=0.75 and fully
487 developed incoming turbulent flow) is larger than the one observed for some high-relative-submergence
488 (D/h>4) obstacles of cylindrical and non-cylindrical shape. For example, Chang and Constantinescu (2020)
489 predicted St_w=0.15-0.16 for porous cylinders with D/h=4, AR=0.14 and fully-developed incoming turbulent
490 flow, while Okamoto and Sunabashiri (1992) and Okamoto and Uemura (1991) reported $St_w \approx 0.22$-0.23 for
491 cylinders with AR=1 and a thin boundary layer at the location of the cylinder. All these values are for subcritical
492 cylinder Reynolds numbers. For same value of AR, the shape of the obstacle can strongly modify St_w. For
493 example, Martinuzzi and AbuOmar (2003) reported St_w=0.33 for a pyramid with AR=1. This value is very close

494 to the one predicted in the present study for a non-filtering mussel. For a square cylinder with AR=0.5 and a
495 thin incoming boundary layer, Sattari et al. (2010) reported St_w=0.33. Hajimirzaie and Buchholz (2013) reported
496 St≈0.185 for semi-ellipsoids with AR=0.67-0.89, D/h≈4 and a thin boundary layer at the location of the obstacle.
497
498 Given that the shape of the emerged part of the mussel in the present study is relatively close to that of a semi-
499 ellipsoid, some discussion is needed on the possible reasons for the large discrepancy between the dominant
500 wake frequency predicted by the present simulation (St_w=0.32) and that observed past semi-ellipsoids with a
501 similar AR value. It is relevant to mention that in the same semi-ellipsoid experiments, Hajimirzaie and
502 Buchholz (2013) reported St_w≈0.35 for D/h≈1 where the anti-symmetric mode dominates. There are several
503 differences in the flow conditions and geometry that can favor a stronger anti-symmetric mode for high D/h
504 values. The asymmetry of the two sides of the shell means one horizontal SSL is stronger than the other (e.g.,
505 circulation of one leg of the same vortex tube is generally larger on one side of the mussel compared to the other
506 side). This increases the asymmetry of the interactions between the horizontal SSLs and can also modify the
507 frequency of these interactions. Moreover, the incoming flow was fully developed in the present simulations.
508 This means more energetic eddies are hitting the mussel and its SSL. These disturbances are random and favor
509 the anti-symmetric mode.
510
511 However, the main reason for the variation in St_w is due to the shape of the frontal part of the mussel. Figure 1c
512 shows that the frontal part is characterized by a pyramid-like shape in the $\theta=0^0$ cases. By contrast, in the case
513 of reversed flow ($\theta=180^0$), the frontal part is much more vertical and closer to a semi-ellipsoid shape. The
514 dominant wake frequency for this case is St_w=0.20, nor far from the value (St≈0.185) measured by Hajimirzaie
515 and Buchholz (2013). This large change in St_w between $\theta=0^0$ and $\theta=180^0$ is not related to a change in the flow
516 physics, as the interactions of the legs of the vortex tubes remain qualitatively similar. The main difference is
517 that the siphons are situated inside the recirculatory flow region in the $\theta=180^0$ case and outside it in the $\theta=0^0$
518 cases. The present study concentrates on the $\theta=0^0$ cases because, as mentioned in the introduction, in the field
519 mussels are mostly oriented with their siphons pointing upstream rather than downstream.
520
521 Table 1 provides information on how St_w varies with the main flow and geometrical parameters for $\theta=0^0$. For
522 constant h/d and U_0, St_w increases with increasing VR (e.g., from 0.32 for VR=0 to 0.39 for VR=0.7). For
523 constant h/d and Q_e, St_w increases with increasing U_0. Finally, for constant U_o and Q_e, St_w decreases with
524 decreasing h/d or increasing D/h. In terms of the nature of the wake shedding, the increase in VR acts toward
525 damping the symmetrical mode. As for the VR=0, h/d=0.5 case, the velocity power spectrum in the VR=0.7,
526 h/d=0.5 case (e.g., see Fig. 13b) contain a secondary peak at $St=2St_w$ that corresponds to the advection of the
527 vortex tubes in the downstream part of the SSL. A secondary peak is also present at a lower frequency
528 ($St\approx0.2\approx St_w/2$). This frequency seems to be associated with the symmetric mode but, as opposed to the VR=0,
529 h/d=0.5 case, it is much less energetic compared to St_w. Examination of the instantaneous vorticity fields in

horizontal planes for the VR=0.7, h/d=0.5 case confirms that, at most time instances, the interactions of the horizontal SSLs are asymmetrical (e.g., see Fig. 14b-c). Even at time instances when the interactions of the horizontal SSLs are limited to those between the legs of the same vortex tube (e.g., Fig. 14a), the vorticity field is less symmetric compared to the non-filtering case.

5 MUSSEL STABILITY

The stability of the partially burrowed mussel is mainly a factor of its capacity to avoid displacement from the bed by the flow. Mussel stability increases with decreasing drag forces acting on the emerged part of the shell and with decreasing local scour developing around the shell that can further expose part of the mussel's body. The effects of the main geometrical and flow parameters on the nondimensional streamwise drag forces and sediment entrainment mechanisms are discussed next.

5.1 Drag forces

The main contributor to the streamwise drag force, F_x, acting on the mussel is the form drag. Figure 15 visualizes the pressure distribution on the exposed part of the mussel's shell and the bed surface. The largest pressures are induced on the front side of the shell where the incoming flow decelerates while being deflected around the two sides of the mussel. Interestingly, the lowest pressures are not recorded at the back of the mussel but rather just downstream of the separation line.

Table 3 Mean streamwise drag coefficient, C_d^{mean} and the root mean square (rms) of the streamwise drag coefficient, C_d^{rms} as a function of θ, VR and h/d. Also given are the values of the projected area of the emerged part of the mussel's shell, A.

Θ (°)	VR (-)	h/d (-)	A ×10^4 (m^2)	C_d^{mean} (-)	C_d^{rms} (-)
0	0.13	0.5	9.072	0.282	0.020
0	0.13	0.375	6.064	0.274	0.019
0	0.13	0.25	3.520	0.220	0.016
0	0	0.5	9.072	0.277	0.012
0	0.5	0.5	9.072	0.301	0.014
0	0.7	0.5	9.072	0.311	0.014
0	0.05	0.5	9.072	0.277	0.009
180	0.7	0.5	9.072	0.304	0.018

For constant h/d and U_0, the effect on increasing VR is to reduce the pressure downstream of the separation line and in particular at the back of the mussel (e.g., compare h/d=0.5 cases with VR=0, 0.13 and 0.7 in Fig. 15). This explains the observed monotonic increase of the nondimensional streamwise mean drag coefficient,

$C_D^{mean} = F_x/0.5\rho U_0^2 A$ (A is the projected area of the emerged part of the shell, Table 3) with VR in Fig. 16a. The increase of C_D^{mean} is close to 12% as VR increases from 0 to 0.7. So, increasing Q_e does not result in a significant increase of the capacity of the isolated mussel to avoid displacement by the overflow. Reversing the flow in the channel only slightly reduces the drag force. As expected, the streamwise drag force is decaying with increasing mussel burrowing (Fig. 16b). The main reason is the reduction of the pressure acting at the front of the shell with decreasing h (e.g., compare VR=0.13 cases with h/d=0.5 and 0.25 in Fig. 15). Table 3 also reports the values of the root-mean-square (rms) of the streamwise drag coefficient, C_d^{rms}. These values are less than 10% of C_D^{mean}. Interestingly, for constant h/d and U_0, C_d^{rms} does not increase monotonically with VR but rather peaks for VR=0.13.

5.2 Sediment entrainment mechanisms

Local scour around the mussel is a function of the bed shear stress in the instantaneous flow fields. Given the presence of horseshoe vortices, vortex tubes and other energetic eddies in the near wake, analysis of the mean bed shear stress, $\overline{\tau}$, is not sufficient to characterize sediment entrainment around the mussel. For example, significant local entrainment can occur at locations where $\overline{\tau}$ is less than the threshold value for sediment entrainment if the turbulence is high near the bed (Cheng et al., 2018). A quantitative measure of the capacity of large-scale turbulent eddies to increase the instantaneous bed shear stresses near a certain bed location is the standard deviation of the bed shear stress, τ_{rms}. In fact, in morphodynamics simulations that do not resolve the energetic eddies in the flow, many approaches to estimate the flux of sediment entrained from the bed recommend using an augmented bed shear stress $\overline{\tau}$ +Cτ_{rms} in standard entrainment formulas, where the empirical coefficient C is close to 1 (Sumer et al., 2003; Kraft et al., 2011; Cheng et al., 2018). Figure 17 presents the distributions of $\overline{\tau}/\overline{\tau}_0$ and $\tau_{rms}/\overline{\tau}_0$ for representative cases, where $\overline{\tau}_0$ is the mean bed shear stress in the approach flow. As the simulations resolve the viscous sublayer, the bed shear stress is estimated as $\bar{\tau}/\rho U_0^2 = (\frac{1}{Re}\frac{u_m/U_0}{n_1/d})$ where u_m is the velocity magnitude in a plane parallel to the channel bed situated at a distance n_1 from it. To estimate τ_{rms}, the square root of the TKE in the same plane replaces u_m.

Qualitatively, the distributions of $\overline{\tau}/\overline{\tau}_0$ are remarkably similar among the different simulations. These distributions also present some important differences with those observed past emerged and submerged, surface-mounted bluff bodies like cylinders of circular or rectangular shape (Kirkil and Constantinescu, 2009, 2015; Chang et al., 2017). As for the case of cylinders placed on a horizontal surface, the largest $\overline{\tau}/\overline{\tau}_0$ values are induced in the region of high flow acceleration on the outer side of the horizontal SSLs. No large amplification of $\overline{\tau}/\overline{\tau}_0$ is observed beneath the horseshoe vortices and low bed shear stresses are predicted at the back of the mussel (Fig. 17a). Despite the fairly small asymmetry of the two sides of the shell, the distributions of $\overline{\tau}$ behind the mussel are highly asymmetrical in most simulations, with much higher bed shear stresses being induced on the left side if the mussel. It is only for relatively low h/d that the distribution of $\overline{\tau}/\overline{\tau}_0$ becomes fairly symmetrical (see Fig. 17a for h/d=0.25).

The most striking difference with the distributions observed for emerged, surface-mounted obstacles and even for submerged solid cylinders (Kirkil and Constantinescu, 2015; Chang et al., 2017, 2020) is that the near wake region, where in principle the flow should slowly recover, is not a region of relatively low bed shear stress compared to the undisturbed channel flow. This effect is due to the high degree of three dimensionality of the mean flow in the near wake and to the pyramid-like shape of the shell. As the incoming flow is deflected laterally around the shell and over its top, it acquires a fairly-strong vertical velocity component oriented toward the bed starting in the region where the flow separates on the shell (Fig. 11). The regions of negative mean vertical velocity in the z/h=0.5 plane correspond to those of high $\overline{\tau}/\overline{\tau}_0$ in Fig. 17a. These downwelling motions result in the advection of higher streamwise velocity fluid closer to the bed, which explains why $\overline{\tau}/\overline{\tau}_0>1$ over most of the near-wake region. Though similar downwelling regions form in the case of flow past submerged cylinders (Chang et al., 2020), the vertical velocities are smaller and the wake mostly contains regions with $\overline{\tau}/\overline{\tau}_0<1$. For the h/d=0.5, $Q_e=1.66\times10^{-6}$ m^3/s cases, the region defined by $\overline{\tau}/\overline{\tau}_0>1.3$ extends until the end of the computational domain and results suggest that its length is of the order of 10 times the mussel width, b. This has important consequences not only for the development of scour in the wake of the mussel but also for the deposition of particulates.

The distributions of $\tau_{rms}/\overline{\tau}_0$ in Fig. 17b generally contain two regions of strong amplification of τ_{rms}. The first one is due to the oscillations of the horseshoe vortices. Except for relatively high levels of mussel burrowing (h/d≤0.375), for which the horseshoe vortex system is steady, the horseshoe vortices are subject to quasi-periodic oscillations. During these oscillations, merging between the primary and secondary vortices occurs, similar to what is observed for a laminar horseshoe vortex during the amalgamation regime (Kirkil and Constantinescu, 2012). The Strouhal number associated with a full oscillatory cycle is close to constant ($St_H=f_Hb/U_0=0.19$ for all $\theta=0^0$ simulations with h/d=0.5, Table 1). The oscillatory movements of the cores of the horseshoe vortices also explain why the pressure rms fluctuations in Fig. 5 display a two-peak structure in front of the mussel. This is different from the case for surface-mounted bluff bodies at high Reynolds numbers where the two peaks are due to bimodal oscillations of the primary horseshoe vortex (Kirkil and Constantinescu, 2015). The second region of high $\tau_{rms}/\overline{\tau}_0$ in Fig. 17b is situated at the back of the mussel, close to y/d=0. This second region has a direct correspondent in the region of high TKE present at z/h=0.5 in Fig. 7b. Animations show that the interactions between the two legs of the vortex tubes generate energetic eddies and some of these eddies are entrained into the region where the flow is oriented toward the back of the shell. This is the main mechanism for the amplification of τ_{rms} in this region.

For constant h/d and U_0, the levels of $\overline{\tau}/\overline{\tau}_0$ in the near wake first decrease as VR increases from 0 to 0.13 and then start increasing with increasing VR. The same is true for the size of the region of high $\tau_{rms}/\overline{\tau}_0$ at the back of the mussel (see simulation results for VR=0, 0.13 and 0.7 in Fig. 17). The effect of increasing U_0 for constant

h/d and Q_e is to reduce both $\overline{\tau}/\overline{\tau}_0$ and $\tau_{rms}/\overline{\tau}_0$ (see results for VR=0.13 and VR=0.05 in Fig. 17). The effect of decreasing h/d for constant VR and U_0 is to reduce $\overline{\tau}/\overline{\tau}_0$ and $\tau_{rms}/\overline{\tau}_0$ in the near wake and on the sides of the mussel. The fact that the horseshoe vortices stop oscillating explains why the amplification of τ_{rms} around the front side of the mussel is negligible in the VR=0.13, h/d=0.25 simulation (Fig. 17b).

6. SCALAR TRANSPORT

Several studies have demonstrated that mussels ingest relatively large amounts of phytoplankton (Haag, 2012). As a result, mussels play an important role in increasing water clarity. One can think of the uniform incoming concentration of phytoplankton as being represented by a scalar with zero concentration, and of the plankton-depleted water entering the channel through the excurrent siphon as being represented by a constant concentration, C_0. Such an 'inverse concentration' approach was also used experimentally to investigate nutrient depletion and distribution of plankton over mussel beds (Monismith et al., 1990; Crimaldi et al., 2007). The constant concentration scalar corresponds to colored dye introduced inside the excurrent siphons in the experiments. The distributions of the mean nondimensional concentration, C/C_0, and its rms fluctuations, C'/C_0, in the y/d=0 plane are shown in Fig. 18 for representative cases. The jet trajectory aligns fairly rapidly with the streamwise direction and the scalar diffusion in the vertical direction takes place mostly in between the channel bed and the top of the mussel. An increase in the excurrent jet discharge, Q_e, increases the size of the regions of high C/C_0 and C'/C_0. This is the main reason why relatively high scalar concentration fluid penetrates up to the channel bed in the VR=0.7, h/d=0.5, case. For constant VR and U_0, a decrease in h/d increases the penetration length of the core of high concentration fluid. A similar effect is observed for the region of high C' that increases its length by about 25% as h/d decreases from 0.5 to 0.25.

At a more fundamental level, the excurrent jet dynamics is a complex case of a jet in cross flow. This similarity was already pointed out by O'Riordan et al. (1993, 1995). However, as opposed to the canonical case of a round jet introduced in a channel through its bottom surface (Mahesh, 2013), the exit of the jet is situated some distance above the channel bed and the exposed part of the shell induces the formation of streamwise base vortices regardless of the presence or absence of active filtering (Fig. 9). Due to the asymmetry of the shell, only one vortex is observed at larger distances from the shell. Some of the usual coherent structures observed in the canonical case are absent, or present only in the (VR=0.7) simulation with a large discharge of the excurrent jet. For example, there is no horseshoe vortex forming on the outer side of the jet as it exits the excurrent siphon simply because there is no horizontal surface surrounding the siphon. The pair of counterrotating vortices that is responsible for the kidney-shape of the jet cross section in the canonical case (e.g., see Yuan and Street, 1998; Muppidi and Mahesh, 2006) is observed only in the VR=0.7 simulation. For the low-velocity-ratio jets (VR<1) considered here, large-scale hairpin vortices are generally observed at low Reynolds numbers (Acarlar and Smith, 1987; Sau and Mahesh, 2008). In the case of the excurrent jet, the top side of the vortex tubes shed in the SSL are quickly stretched such that these tubes resemble large hairpin structures in the near wake (Fig. 3b).

In the present simulations, the jet cross section is close to circular, or slightly ellipsoidal, once its trajectory becomes close to parallel to the bed (e.g., see x/d=1 plane in Fig. 19). This is the case even for the VR=0.7 simulation where weak counter-rotating tip vortices are present close to the excurrent siphon ($x/d<0.8$) and the line defined by their axes is strongly tilted with respect to the horizontal (see x/d=0.55 plane in Fig. 9c). Though the axes of the base vortices are not always close to the jet centerline, they influence the streamwise evolution of the jet. This is especially the case for the high VR and high h/d cases where only one base vortex is observed at larger distances from the shell (e.g., for $x/d>0.8$). In the low VR cases (e.g., Fig. 19c for VR=0.05, h/d=0.5), the jet cross section remains close to circular until the end of the computational domain. The same is true for the VR=0.13, h/d=0.25 case (Fig. 19d). By contrast, in the VR=0.7, h/d=0.5 case (Fig. 19b), the jet cross section is more ellipsoidal and its major axis is tilted with respect to the vertical, consistent with the direction of rotation of the main base vortex. A weaker tilting is also observed in the VR=0.13, h/d=0.5 case near the end of the computational domain (see x/d=5 plane in Fig. 19a).

The axis of the jet is defined as the location of the maximum mean concentration, C_{max}, in the cross section and is used to describe the jet trajectory in the mean flow. The streamwise variation of the vertical position of the jet centerline and of its maximum nondimensional concentration, C_{max}/C_0, are shown in Figs. 20a and 20b, respectively. Qualitatively, the jet trajectories are similar in all cases. Due to its initial vertical momentum as it exits the siphon, the jet moves initially upwards. As the jet changes direction, its centerline reaches a maximum height and then it starts approaching the channel bed. For all cases, the jet trajectory reaches a regime where its centerline approaches the bed at a close to constant angle. This regime starts around $x/d_j=10$, where d_j is the jet diameter as it exits the excurrent siphon.

The maximum vertical penetration of the jet away from the channel bottom is an important variable because of the water quality implications in terms of nutrient transport and water clarity. With respect to the position of the excurrent siphon ($z/d_j=0$ in Fig. 20a), the vertical penetration distance increases monotonically with increasing VR (e.g., from about $0.7d_j$ for VR=0.05 to $1.7d_j$ for VR=0.7) and is fairly insensitive to h/d even though a small increase with decreasing h/d is observed in the VR=0.13 simulations. For constant h/d, the close to constant angle at which the jet centerline approaches the channel bed for $x/d_j>10$ decreases with increasing VR. For constant VR, the angle decreases monotonically with decreasing h/d, as the jet evolution is stronger affected by the channel bed for low h/d. Over the same $x/d_j>10$ region, the peak concentration in the cross section, $C_{max}(x/d_j)/C_0$, decreases faster with increasing VR for constant h/d (Fig. 20b). For constant VR, the decay of C_{max}/C_0 with x/d_j is qualitatively similar in the simulations performed with different values of h/d. Still, at a given streamwise location, C_{max} increases with decreasing h/d. This is because a jet that penetrates over a longer streamwise distance before interacting with the channel bed mixes more rapidly with the surrounding faster-moving flow.

To characterize entrainment into the jet, Fig. 20c compares the streamline variations of the nondimensional volume flux of the jet, $Q_j(x/dj)/Q_{j0}$, where Q_{j0} is the scalar flux as the jet leaves the excurrent siphon. To estimate Q_j in a given cross section, one needs to distinguish between jet fluid and cross flow fluid. This is done using the procedure proposed by Yuan and Street (1998) who calculated a threshold value for the scalar concentration, C_{min}. Jet fluid corresponds to fluid with $C>C_{min}$. The value of C_{min} is determined as that for which the relative difference between the scalar flux generated by the jet estimated using a threshold value C_{min} and using no threshold value is less than 1%. For the computational domain used, this procedure yielded a threshold value $C_{min}=0.0001C_0$. At a given streamwise location, Q_j/Q_{j0} increases monotonically with increasing VR for constant h/d. This is rather expected, as an increase of VR means that the mean shear between the jet region and the surrounding flow is also larger. This enhances the production of turbulence by mean shear and also mixing. Over the regime where the jet axis slowly approaches the bed at a close to constant angle ($x/d_j>10$), the entrainment rate (e.g., the rate of increase of Q_j/Q_{j0}) increases with increasing VR. If VR and U_0 are kept constant, then Q_j/Q_{j0} increases monotonically with increasing h/d at a given streamwise location. This is because a jet exiting at a higher elevation with respect to the channel bed is in contact with higher-velocity fluid. Which increases mixing and entrainment. For constant VR and U_0, the rate of increase of Q_j/Q_{j0} for $x/d_j>10$ increases with increasing h/d. The main reason is that the core of the jet interacts less with the bottom boundary layer for higher values of h/d. It is also worth mentioning that plotting Q_j/Q_{j0} vs x/d_j in linear-log scale for $x/d_j>10$ results in a close to linear relationship between these two variables for all cases. The slope of the best fit increases with h/d for constant VR and decreases with VR for constant h/d.

7. FINAL DISCUSSION AND CONCLUSIONS

Compared to flow past surface-mounted obstacles, the flow past partially-burrowed, freshwater musels is characterized by local mass exchange between the mussel and the overflow through the incurrent and excurrent siphons. The passive contribution due to the exposed part of the mussel's shell is qualitatively similar to flow past submerged obstacles of regular shape (e.g., hemispheres, semi-ellipsoids, pyramids, cones). Given that the flow disturbance around the incurrent siphon is fairly reduced, the active contribution on the near-bed flow is mainly due to the flow disturbance associated with the excurrent siphon jet. This is a complex case of a low velocity ratio (VR<1) jet in cross flow, where the jet exit is situated above the channel bed and the jet develops into the wake of the emerged part of the mussel. The paper discusses the critical role played by large-scale turbulence generated around the mussel and, in particular, the dynamics of the streamwise-oriented base vortices and of the vortex tubes that are forming in the separated shear layer (SSL). Due to the shape of the emerged part of the mussel's shell, the vortex tubes have an U-shape that follows the separation line on the shell.

One of the main findings of the present study is that the counter-rotating base vortices play a major role in the wake dynamics. As opposed to symmetrical obstacles of regular shape, where the coherence of the two vortices is comparable, the slight assymetry of the two valves forming the shell results in one of these vortices loosing its coherence at about 1b from the back of the mussel, where b is the maximum width of the emerged part of the

737 shell. The other vortex maintains its coherence for much longer streamwise distances. Due to the base vortices,
738 strong downwelling is observed in two regions behind the shell. On the side of the more coherent base vortex,
739 the flow downwelling region is much larger. For the largest value of VR, this region extends for about 3b from
740 the back of the shell. The base vortices also induce strong flow upwelling in between the horizontal SSLs. The
741 end result is that higher streamwise velocity fluid is advected near the bed inside the regions of flow
742 downwelling. This induces a substantial increase of the mean bed shear stress compared to the value in the
743 surrounding undisturbed flow. So, a large part of the near-wake region, rather then being a region of lower bed
744 shear stress, is a region where sediment erosion and entrainment of particulates and matter from the substrate
745 are enhanced. Another interesting finding is that the total streamwise drag force acting on the shell increases
746 with increasing VR and filtering discharge. This means that for isolated mussels filtering cannnot be used as a
747 way to increase mussel stability. However, this finding does not automatically apply for mussel beds where
748 wake-to-mussel interactions are controlling the flow over the substrate.
749
750 Another important finding is that despite the fact that wake vortex shedding is mainly associated with
751 interactions between the two legs of the same vortex tube, the antisymmetric mode dominates and its strength
752 increases with increasing VR. For same flow conditions, the direction of the incoming flow (upstream oriented
753 siphons vs. downstream oriented siphons) can greatly change the value of the dominant wake shedding
754 frequency. This means that quantitative information obtained from studies conducted with surface-mounted
755 obstacles of regular, symmetrical shape is of limited use for describing flow past partially burrowed freshwater
756 mussels even under non-filtering conditions.
757
758 Given the fact that the excurrent siphon transports plankton-depleted water, mussel filtering modifies the vertical
759 profile of the phytoplankton concentration in the channel. Understanding mixing between the jet and the
760 surrounding near-bed flow is also important to quantify nutrient availability and dispersal. Present simulations
761 showed that the vertical overshot of the jet over the excurrent siphon level and the volume flux of the jet increase
762 with increasing height of the emerged part of the mussel, h. For sufficiently high h and high VR, the main base
763 vortex has a noticeable influence on the downstream development of the excurrent siphon jet; its cross section
764 becomes noncircular and its major axis tilts with respect to the vertical.
765
766 The present study showed that the near-bed flow structure around an isolated freshwater mussel is significantly
767 affected by relatively subtle changes in the main flow and geometrical parameters. Future research will include
768 studying the effect of the angle of attack. During floods, the mean flow direction can change rapidly before
769 mussels can reorient themselves parallel to the flow. The capacity of the flow to displace the mussels increases
770 rapidly with the angle of attack. The present work considered only the simplest case of a constant filtering
771 discharge. Availability of more detailed information on the temporal variability of the filtering discharge from
772 live mussel studies can be used to perform simulations with more realistic siphonal flows. Finally, mussels are
773 often present in gravel beds where the near-bed turbulence levels in the incoming flow are much larger. The

774 effects of large-scale bed roughness on the near-wake flow structure and drag forces acting on the mussel are
775 largely unknown.
776
777 **Acknowledgments**
778 The data can be accessed at http://doi.org/10.5281/zenodo.*****. The authors would like to thank Dr. B.
779 Sansom and Prof. S. Bennett from SUNY Univ. at Buffalo for providing a model of the mussel surface,
780 performing the validation experiments, providing the data used to validate the numerical model as part of a
781 collaborative US National Science Foundation project and for stimulating discussions. This work was supported
782 by the EAR Hydrologic Sciences Program of the US National Science Foundation under GRANT No. 1659518.
783 Any opinions, findings, and conclusions or recommendations expressed in this material are those of the authors
784 and do not necessarily reflect the views of the U.S. National Science Foundation.
785
786 **References**

787 Acarlar, M. S., & Smith, C. R. (1987). A study of hairpin vortices in a laminar boundary layer. Part 1. Hairpin vortices
788 generated by a hemisphere protuberance. *Journal of Fluid Mechanics*, 175, 1-41.
789 Allen, D. C., & Vaughn, C. C. (2009). Burrowing behavior of freshwater mussels in experimentally manipulated
790 communities. *Journal of the North American Benthological Society*, 28(1), 93-100.
791 Atkinson, C.L., C.C. Vaughn, K.J. Forshay, & J.T. Cooper (2013). Aggregated filter-feeder consumers alter nutrient
792 limitation: Consequences for ecosystem and community dynamics. *Ecology*, 94, 1359-1369.
793 Butman, C. A., Fréchette, M., Geyer, W. R., & Starczak, V. R. (1994). Flume experiments on food supply to the blue
794 mussel Mytilus edulis L. as a function of boundary‐layer flow. *Limnology and oceanography*, 39(7), 1755-1768.
795 Castro, I., Vosper, S., Paisley, M., & Hayden, P. (2001). Vortex shedding behind tapered obstacles in neutral & stratified
796 flow. *Dynamics of atmospheres and oceans*, 34(2-4), 145-163.
797 Chang, K.S., Constantinescu, G. & Park, S.O. (2007). Assessment of predictive capabilities of Detached Eddy Simulation
798 to simulate flow and mass transport past open cavities, *ASME Journal of Fluids Engineering*, 129(11), 1372-1383.
799 Chang, W.Y., Constantinescu, G. & Tsai, W.Y. (2017). On the flow and coherent structures generated by an array of rigid
800 emerged cylinders place in an open channel with flat and deformed bed, *Journal of Fluid Mechanics*, 831, 1-40.
801 Chang, W.Y., Constantinescu, G. & Tsai, W.F. (2020). Effect of array submergence on flow and coherent structures
802 through and around a circular array of rigid vertical cylinders. *Physics of Fluids*, 32, 035110.
803 Cheng, Z., Koken, M., & Constantinescu, G. (2018). Approximate methodology to account for effects of coherent
804 structures on sediment entrainment in RANS simulations with a movable bed and applications to pier scour. *Advances*
805 *in Water Resources*, 120, 65-82.
806 Constantinescu, G. S., & Squires, K. D. (2003). LES and DES investigations of turbulent flow over a sphere at Re=
807 10,000. *Flow, Turbulence and Combustion*, 70(1-4), 267-298.
808 Constantinescu, G., Chapelet, M.C., & Squires, K.D. (2003). Turbulence modeling applied to flow over a sphere, *AIAA*
809 *Journal*, 41(9), 1733-1743
810 Constantinescu, G., Miyawaki, S. & Liao, Q. (2013). Flow and turbulence structure past a cluster of freshwater mussels.
811 *Journal of Hydraulic Engineering* 139(4): 347-358.

812 Crimaldi, J. P., Thompson, J. K., Rosman, J. H., Lowe, R. J., & Koseff, J. R. (2002). Hydrodynamics of larval settlement:
813 the influence of turbulent stress events at potential recruitment sites. *Limnology and Oceanography*, 47(4), 1137-
814 1151.
815 Crimaldi, J. P., Koseff, J. R., & Monismith, S. G. (2007). Structure of mass and momentum fields over a model
816 aggregation of benthic filter feeders. *Biogeosciences,* 4, 269–282.
817 Di Maio, J., & Corkum, L. D. (1997). Patterns of orientation in unionids as a function of rivers with differing hydrological
818 variability. *Journal of Molluscan Studies*, 63(4), 531-539.
819 Engelhardt C, Krüger A., Sukhodolov A, & Nicklisch A. (2004). A study of phytoplankton spatial distributions, flow
820 structure and characteristics of mixing in a river reach with groynes. *Journal of Planktonic Research*, 26, 1351-1366
821 Haag, W. R. (2012). North American freshwater mussels: natural history, ecology, and conservation. *Cambridge*
822 *University Press*.
823 Hajimirzaie, S. M., Wojcik, C. J., & Buchholz, J. H. (2012). The role of shape and relative submergence on the structure
824 of wakes of low-aspect-ratio wall-mounted bodies. *Experiments in Fluids*, 53(6), 1943-1962.
825 Hajimirzaie, S. M., & Buchholz, J. H. (2013). Flow dynamics in the wakes of low-aspect-ratio wall-mounted
826 obstacles. *Experiments in Fluids*, 54(11), 1616.
827 Horna-Munoz, D. & Constantinescu, G. (2018). A fully 3-D numerical model to predict flood wave propagation and
828 assess efficiency of flood protection measures. *Advances in Water Resources,* 122, 148-165.
829 Horna-Munoz, D. & Constantinescu, G. (2020) 3-D dam break flow simulations in simplified and complex domains.
830 *Advances in Water Resources*, 137, 103510, https://doi.org/10.1016/j.advwatres.2020.103510.
831 Howard, J. K., & Cuffey, K. M. (2003). Freshwater mussels in a California North Coast Range river: occurrence,
832 distribution, and controls. *Journal of the North American Benthological Society*, 22(1), 63-77.
833 Keylock, C. J., Hardy, R. J., Parsons, D. R., Ferguson, R. I., Lane, S. N. & Richards, K. S. (2005). The theoretical
834 foundations and potential for large eddy simulation in fluvial geomorphic and sedimentological research. *Earth*
835 *Science Review*, Vol. 71, 271– 304.
836 Keylock, C.J., Constantinescu, G. & Hardy, R.J. (2012). The application of computational fluid dynamics to natural river
837 channels: Eddy resolving versus mean flow approaches. *Geomorphology*, 179, 1-20,
838 http://dx.doi.org/10.1016/j.geomorph.2012.09.006.
839 Kirkil, G. & Constantinescu, G. (2009). Nature of flow and turbulence structure around an in-stream vertical plate in a
840 shallow channel and the implications for sediment erosion. *Water Resources Research*, 45, W06412,
841 doi:10.1029/2008WR007363.
842 Kirkil, G. & Constantinescu, G. (2010). Flow and turbulence structure around an in-stream rectangular cylinder with
843 scour hole. *Water Resources Research,* 46, W11549, doi:10.1029/2010WR009336.
844 Kirkil, G. & Constantinescu, G. (2012), The laminar necklace vortex system and wake structure in a shallow channel flow
845 past a bottom-mounted circular cylinder, *Physics of Fluids,* 24, 073602.
846 Kirkil, G. & Constantinescu G. (2015). Effects of cylinder Reynolds number on the turbulent horseshoe vortex system
847 and near wake of a surface-mounted circular cylinder. *Physics of Fluids,* 27, 075102.
848 Koken, M., Constantinescu G. & Blanckaert, K. (2013). Hydrodynamic processes, sediment erosion mechanisms, and
849 Reynolds-number-induced scale effects in an open channel bend of strong curvature with flat bathymetry, *J.*
850 *Geophysical Research-Earth Surface,* 118, 2308-2324.

Kraft, S., Wang, Y., & Oberlack, M. (2011). Large eddy simulation of sediment deformation in a turbulent flow by means of level-set method. *Journal of Hydraulic Engineering*, 137(11), 1394-1405.

Kumar, S. S., Kozarek, J., Hornbach, D., Hondzo, M., & Hong, J. (2019). Experimental investigation of turbulent flow over live mussels. *Environmental Fluid Mechanics*, 19(6), 1417-1430.

Lohrer, A. M., Thrush, S. F., & Gibbs, M. M. (2004). Bioturbators enhance ecosystem function through complex biogeochemical interactions. *Nature*, 431(7012), 1092-1095.

Mahesh, K. (2013). The interaction of jets with crossflow. *Annual review of fluid mechanics*, 45, 379-407.

Martinuzzi, R. J., & AbuOmar, M. (2003). Study of the flow around surface-mounted pyramids. *Experiments in fluids*, 34(3), 379-389.

Mason, P. J., & Morton, B. R. (1987). Trailing vortices in the wakes of surface-mounted obstacles. *Journal of Fluid Mechanics*, 175, 247-293.

Monismith, S. G., Koseff, J. R., Thompson, J. K., O'Riordan, C. A. & Nepf, H. M. (1990). A study of model bivalve siphonal currents. *Limnology and Oceanography*, 35(3), 680-696.

Muppidi, S., & Mahesh, K. (2006). Passive scalar mixing in jets in crossflow. *In 44th AIAA Aerospace Sciences Meeting and Exhibit*, 1098-1196.

Nakato, T., Christensen, J., & Schonhoff, B. (2007). Freshwater mussel survey in pool 16, the Mississippi river, near Fairport, Iowa: Rm 463.5-Rm 464.1. *IIHR Technical Report 464*, The University of Iowa, IIHR-Hydroscience & Engineering.

Okajima, A. (1982). Strouhal numbers of rectangular cylinders. *Journal of Fluid Mechanics*, 123, 379-398.

Okamoto, S. H., & Uemura, N. (1991). Effect of rounding side-corners on aerodynamic forces and turbulent wake of a cube placed on a ground plane. *Experiments in Fluids*, 11(1), 58-64.

Okamoto, S., & Sunabashiri, Y. (1992). Vortex shedding from a circular cylinder of finite length placed on a ground plane, *Journal of Fluids Engineering*, 114(4), 512-521.

O'Riordan, C. A., Monismith, S. G., & Koseff, J. R. (1993). A study of concentration boundary-layer formation over a bed of model bivalves. *Limnology and Oceanography*, 38(8), 1712-1729.

O'Riordan, C. A., Monismith, S. G., & Koseff, J. R. (1995). The effect of bivalve excurrent jet dynamics on mass transfer in a benthic boundary layer. *Limnology and Oceanography*, 40(2), 330-344.

Pattenden, R. J., Turnock, S. R., & Bressloff, N. W. (2002). An experimental and computational study of 3-d unsteady flow features found behind a cylinder. *In Third Fluids Engineering Summer Meeting*, Japan.

Pattenden, R. J., Turnock, S. R., & Zhang, X. (2005). Measurements of the flow over a low-aspect-ratio cylinder mounted on a ground plane. *Experiments in Fluids*, 39(1), 10-21.

Price, R. E., & Schiebe, F. R. (1978). Measurements of velocity from excurring siphons of freshwater clams. *Nautilus*, 92(2), 67-69.

Riisgård, H. U., Jørgensen, B. H., Lundgreen, K., Storti, F., Walther, J. H., Meyer, K. E., & Larsen, P. S. (2011). The exhalant jet of mussels Mytilus edulis. *Marine Ecology Progress Series*, 437, 147-164.

Rodi, W., Constantinescu, G. & Stoesser, T. (2013). Large Eddy Simulation in hydraulics, *IAHR Monograph*, CRC Press, Boca Raton, Florida, USA, Taylor & Francis Group.

Sansom, B. J., Atkinson, J. F., & Bennett, S. J. (2018). Modulation of near-bed hydrodynamics by freshwater mussels in an experimental channel. *Hydrobiologia*, 810(1), 449-463.

Sansom, B.J. (2019). Personal Communication.

Sattari, P., Bourgeois, J. A., & Martinuzzi, R. J. (2010). Turbulent wake of surface-mounted finite aspect ratio bluff bodies. *In ASME conference proceedings* (30811).

Sau, R., & Mahesh, K. (2008). Dynamics and mixing of vortex rings in crossflow. *Journal of Fluid Mechanics*, 604, 389-409.

Savory, E. & Toy, N. (1986). Hemisphere and hemisphere-cylinders in turbulent boundary layers. *Journal of Wind Engineering and Industrial Aerodynamics*, 23, 345-364.

Savory, E., & Toy, N. (1988). The separated shear layers associated with hemispherical bodies in turbulent boundary layers. *In Advances in Wind Engineering*, Elsevier, 291-300.

Shamloo, H., Rajaratnam, N., & Katopodis, C. (2001). Hydraulics of simple habitat structures. *Journal of Hydraulic Research*, 39(4), 351-366.

Spalart, P., and Allmaras, S. (1992). A one-equation turbulence model for aerodynamic flows. *In 30th Aerospace Sciences Meeting and Exhibit*, 439-451.

Spalart, P. (2000). Trends in turbulence treatments. *In Fluids 2000 Conference and Exhibit*, 2306-2314.

Strayer, D. L., Downing, J. A., Haag, W. R., King, T. L., Layzer, J. B., Newton, T. J., & Nichols, S. J. (2004). Changing perspectives on pearly mussels, North America's most imperiled animals. *BioScience*, 54(5), 429-439.

Sumer, B. M., Chua, L. H., Cheng, N. S., & Fredsøe, J. (2003). Influence of turbulence on bed load sediment transport. *Journal of Hydraulic Engineering*, 129(8), 585-596.

Sumner, D., Heseltine, J. L., & Dansereau, O. J. P. (2004). Wake structure of a finite circular cylinder of small aspect ratio. *Experiments in Fluids*, 37(5), 720-730.

Vaughn, C. C., Gido, K. B., & Spooner, D. E. (2004). Ecosystem processes performed by unionid mussels in stream mesocosms: species roles and effects of abundance. *Hydrobiologia*, 527(1), 35-47.

Vaughn, C. C., Nichols, S. J., & Spooner, D. E. (2008). Community and foodweb ecology of freshwater mussels. *Journal of the North American Benthological Society*, 27(2), 409-423.

Wu, P., Horna-Munoz, D., Constantinescu, G. & Quian, Z. (2020). Two-phase flow DES and URANS simulations of pump-intake bay vortices. *Journal Hydraulics Research,* 58(1), 120-132.

Yuan, L. L., & Street, R. L. (1998). Trajectory and entrainment of a round jet in crossflow. *Physics of fluids*, 10(9), 2323-2335.

Zeng, J., Constantinescu, G., Blanckaert, K. & Weber, L. (2008), Flow and bathymetry in sharp open-channel bends: Experiments and predictions, *Water Resources Research*, Vol. 44, W09401.

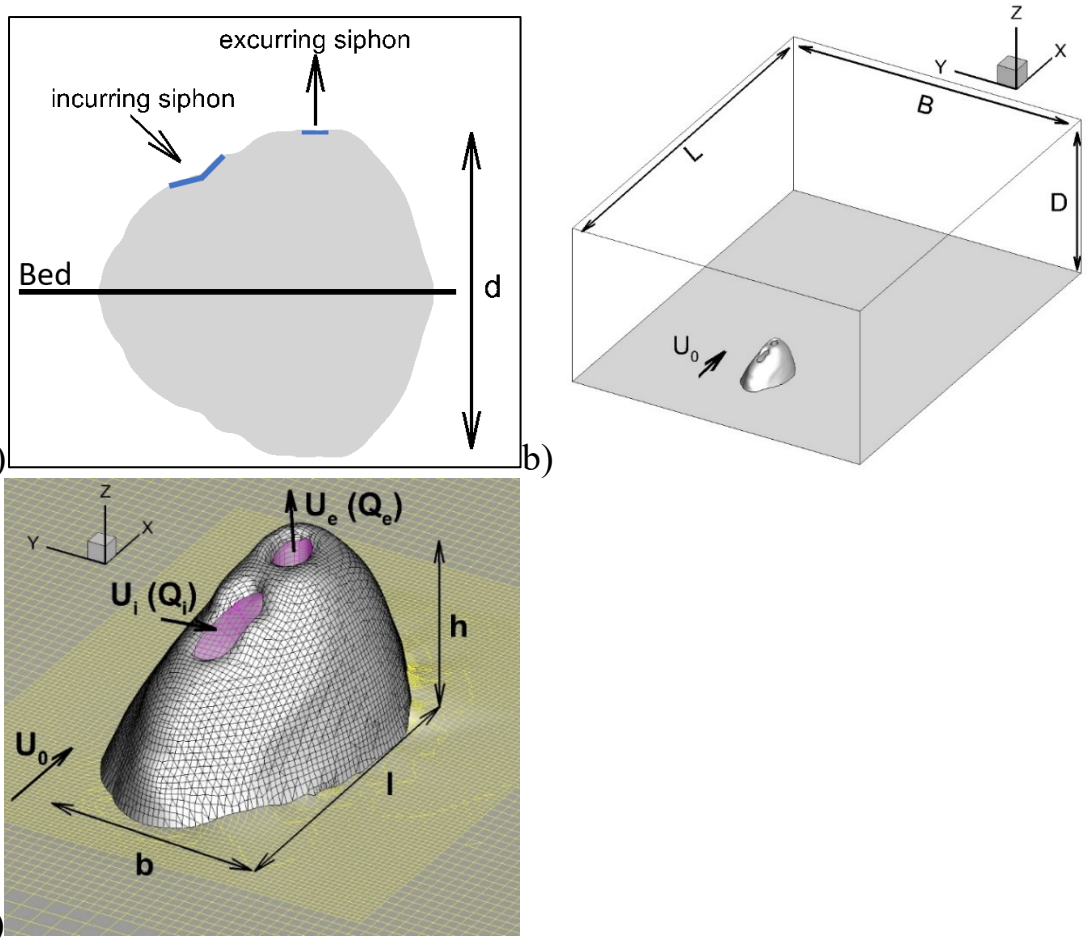

Fig. 1 Sketch of a partially burrowed mussel and general set-up of the numerical simulations. a) sketch showing the mussel's shell with the emerged and burrowed parts and the two siphons; b) computational domain; c) surface mesh on the shell of a partially burrowed mussel (emerged height h=d/2) and on the channel bed. The incoming flow velocity in the channel is U_0, the mussel height is d and the mean velocities and discharges of the flow in the excurrent and incurrent siphons are U_e, Q_e and U_i, Q_i, respectively (Q_i=Q_e).

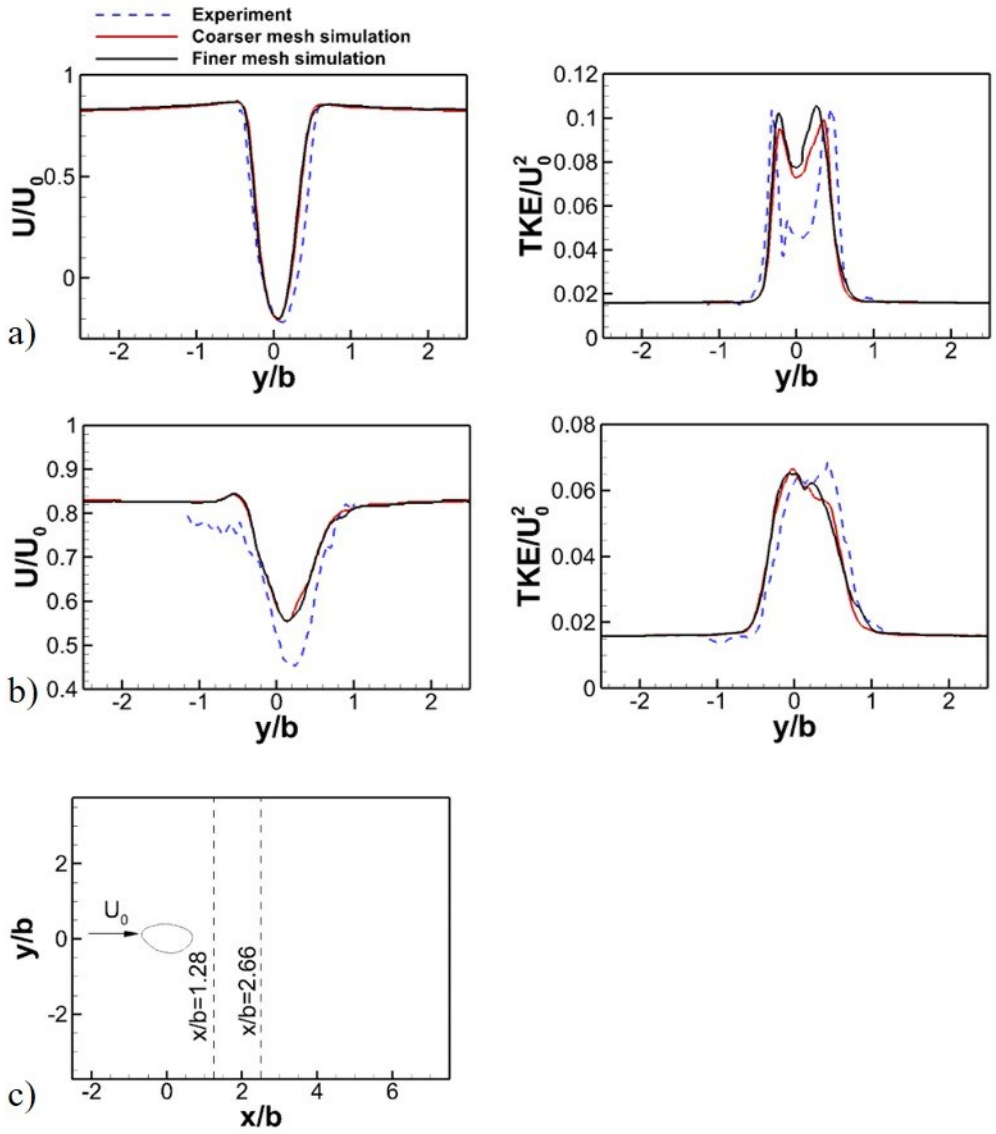

Fig. 2 Comparison between simulation results and experimental measurements (Sansom, 2019) for the nondimensional mean streamwise velocity, U/U_0, and the turbulent kinetic energy, TKE/U_0^2, in the wake of an isolated mussel ($\theta=0^0$, VR=0.0, h/d=0.5, b/d=0.65,U_0=0.3 m/s). Simulation results are reported for a coarser mesh containing about 1.5 million cells and a finer mesh containing about 4 million cells. Spanwise profiles are shown at: a) x/b=1.28 (x=0.05 m), z/h≈0.5 (z=0.015 m); b) x/b=2.56 (x=0.1 m), z/h≈0.5 (z=0.015 m). The sketch in c) shows the positions of the two profiles relative to the mussel.

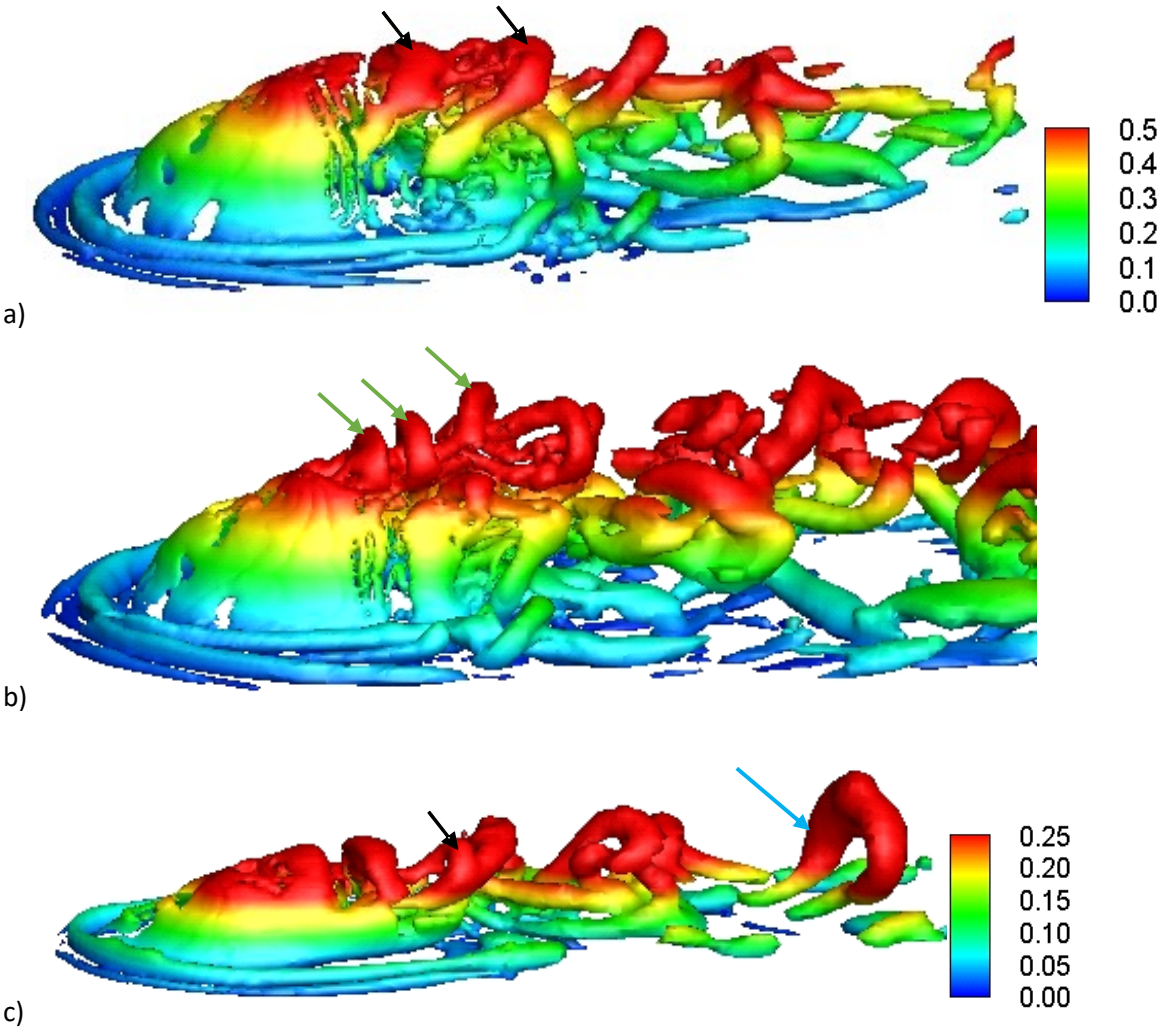

Fig. 3 Visualization of the coherent structures in an instantaneous flow field using the Q criterion ($\theta=0^0$ cases). a) VR=0, h/d=0.5; b) VR=0.7, h/d=0.5; c) VR=0.13, h/d=0.25 The color contours show the vertical distance from the bed, z/d. The black arrows point toward vortex tubes whose tops (heads) are tilted downstream. The green arrows point toward jet shear-layer vortices resembling hairpins. The blue arrow in c) points toward a large-scale hairpin vortex in the near wake whose legs are parallel to the bed.

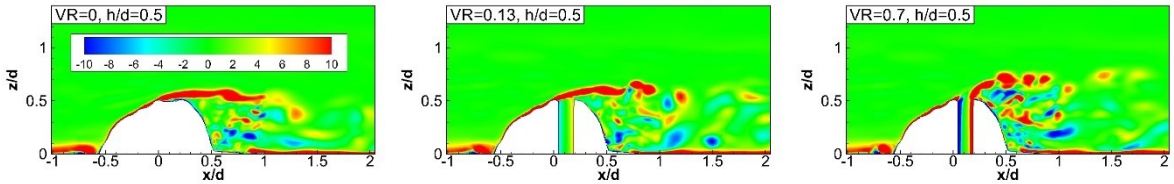

Fig. 4 Instantaneous flow spanwise vorticity, $\omega_y(d/U_0)$ in the vertical y/d=0 plane ($\theta=0^0$ cases). In the VR>0 cases, the y/d=0 plane cuts through the vertical pipe used to advect excurrent-siphon fluid.

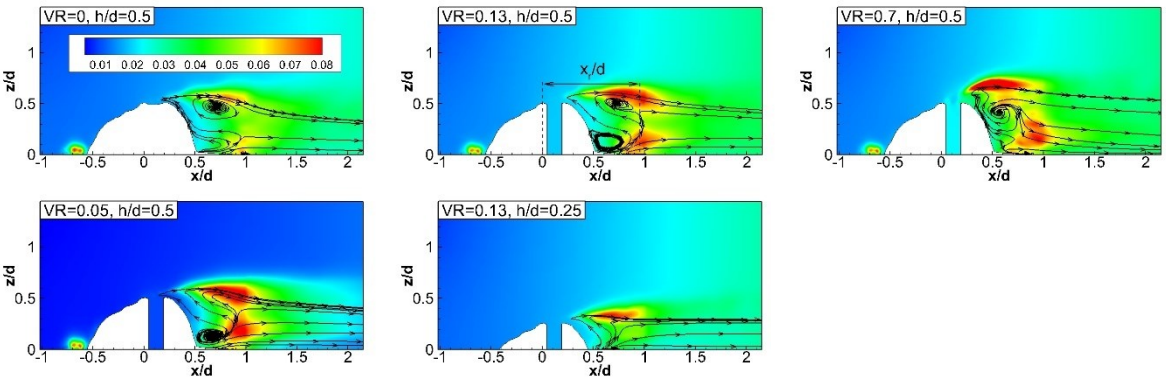

Fig. 5 Mean flow, 2-D streamline patterns behind the mussel and pressure rms fluctuations, $p_{rms}/\rho U_0^2$, in the vertical y/d=0 plane ($\theta=0^0$ cases).

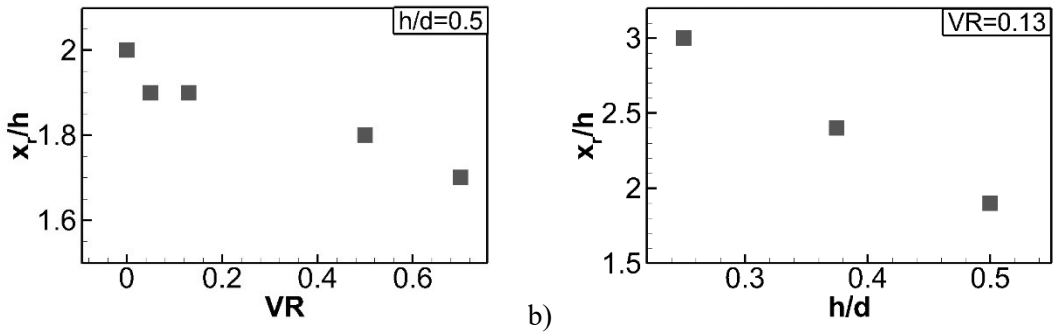

a) b)

Fig. 6 Length of the main region containing recirculation bubbles and upstream moving fluid at the back of the mussel ($\theta=0^0$ cases). a) x_r/h vs. VR for h/d=0.5; b) x_r/h vs. h/d for VR=0.13.

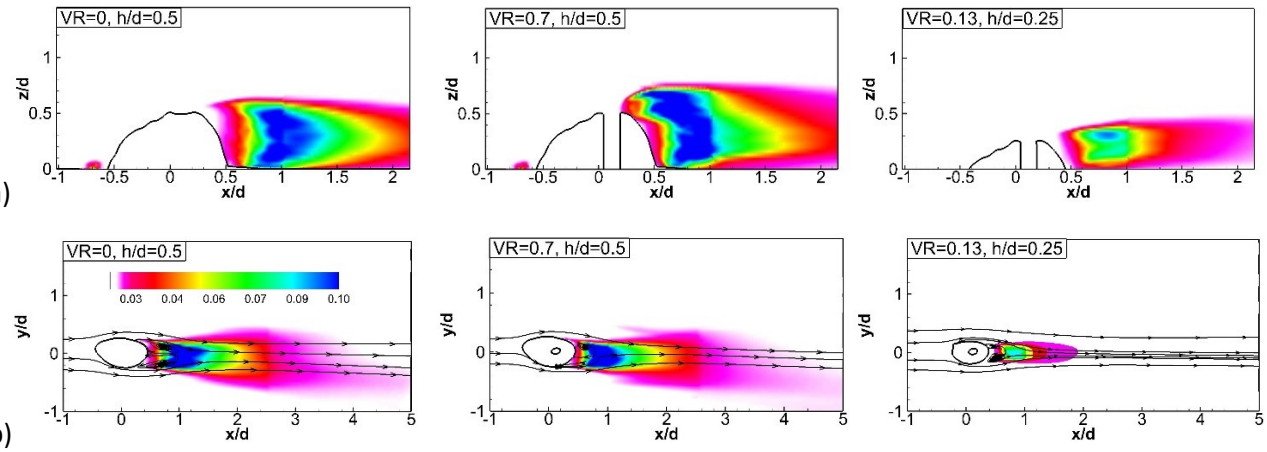

a)

b)

Fig. 7 Turbulent kinetic energy, TKE/U_0^2 ($\theta=0^0$ cases). a) vertical y/d=0 plane; b) horizontal z/h=0.5 plane. Also shown in b) are the 2-D mean streamline patterns. Values of the TKE/U_0^2<0.025 were blanked.

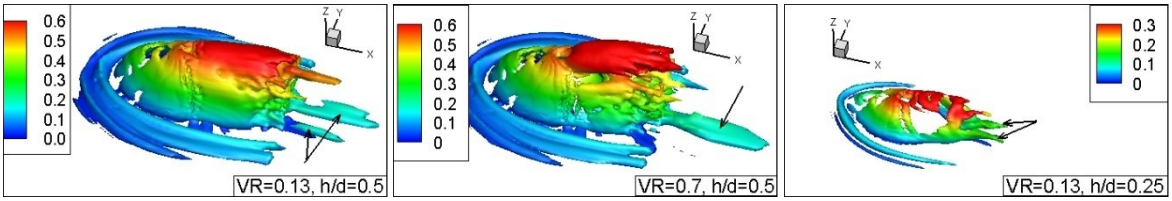

Fig. 8 Coherent structures in the mean flow visualized using the Q criterion ($\theta=0^0$ cases). The black arrows point toward the streamwise-oriented base vortices. Also shown are the horseshoe vortices. The color contours show the vertical distance from the bed, z/d.

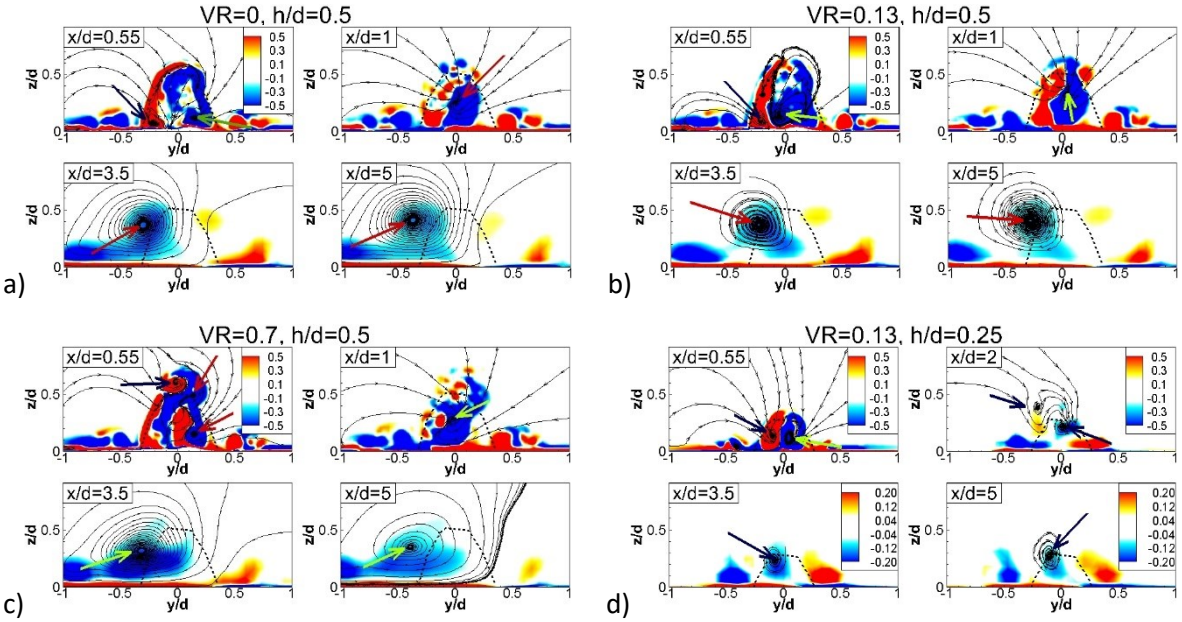

Fig. 9 Mean flow streamwise vorticity, $\omega_x d/U_0$, in x/d=constant planes ($\theta=0^0$ cases). a) VR=0, h/d=0.5; b) VR=0.13, h/d=0.5; c) VR=0.7, h/d=0.5; d) VR=0.13, h/d=0.25. The dotted line shows the projection of the mussel's shell. The arrows point toward the base vortices. In frame c, the x/d=0.55 section also contains two arrows pointing toward the counter-rotating tip vortices.

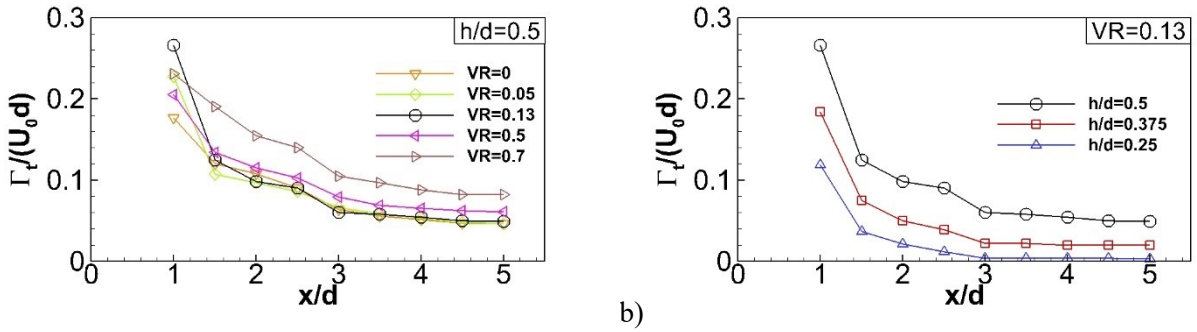

Fig. 10 Total circulation magnitude of the streamwise-oriented, base vortices ($\theta=0^0$ cases). a) Γ_t vs. VR for h/d=0.5; b) Γ_t vs. h/d for VR=0.13.

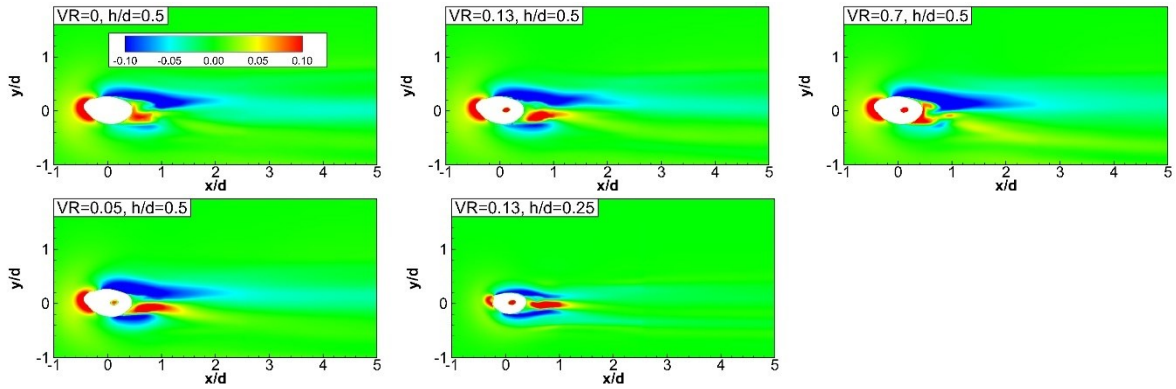

Fig. 11 Mean vertical velocity, w/U_0, in a horizontal plane (z/h=0.5) cutting halfway between the bed and the top of the mussel ($\theta=0^0$ cases).

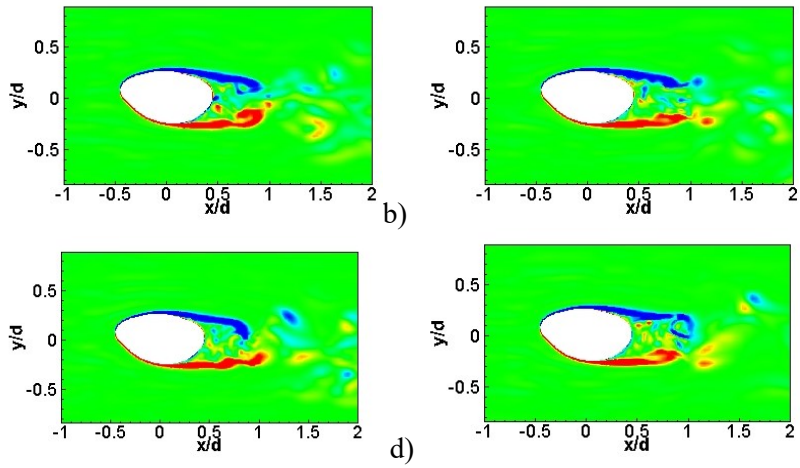

Fig. 12 Instantaneous-flow vertical vorticity, $\omega_z(d/U_0)$, distribution in the z/h=0.5 plane for the $\theta=0^0$, VR=0, h/d=0.5 case illustrating symmetrical (a-b) and anti-symmetrical (c-d) wake shedding.

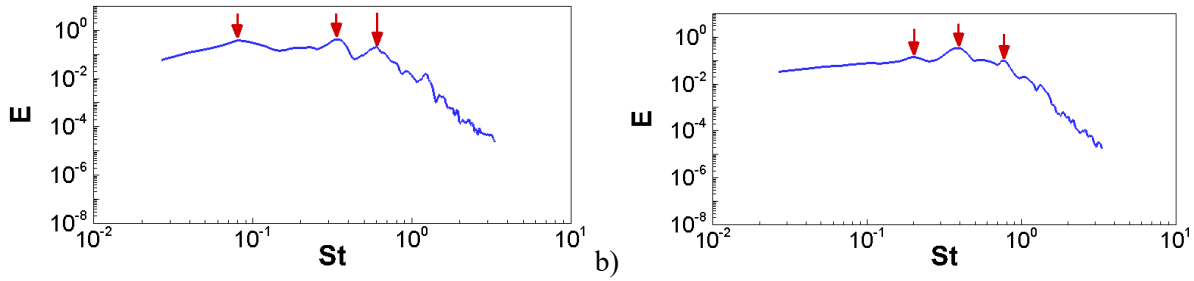

Fig. 13 Power spectrum of streamwise velocity in the near wake region (x/d=2.0; y/d=0.0; z/h=0.25). a) $\theta=0^0$, VR=0, h/d=0.5; b) $\theta=0^0$, VR=0.7, h/d=0.5.

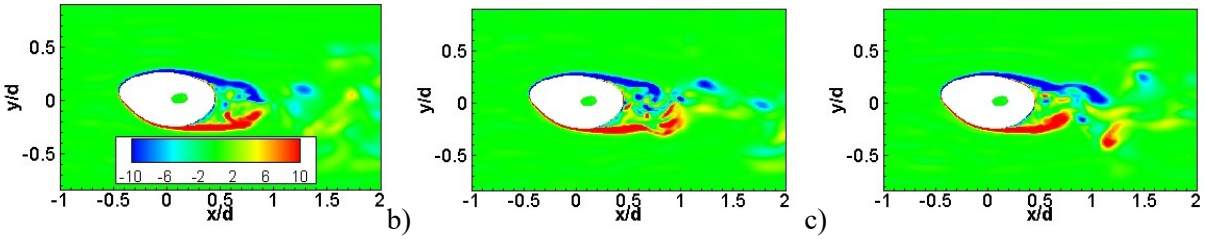

Fig. 14 Instantaneous-flow vertical vorticity, $\omega_z(d/U_0)$, distribution in the z/h=0.5 plane for the $\theta=0^0$, VR=0.7, h/d=0.5 case illustrating symmetrical (a) and anti-symmetrical (b-c) wake shedding.

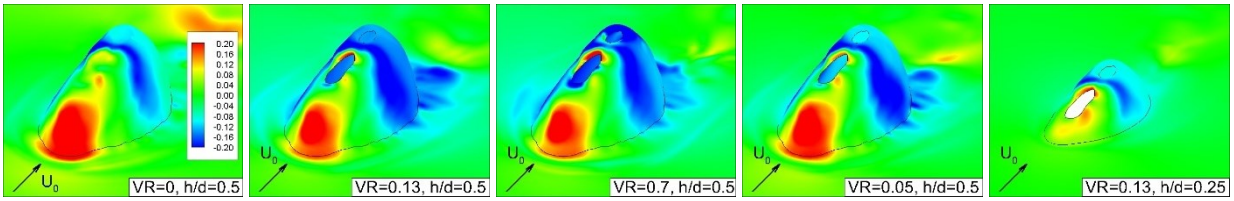

Fig. 15 Mean pressure on the mussel's shell and the channel bed, $p/\rho U_0^2$ (θ=0^0 cases).

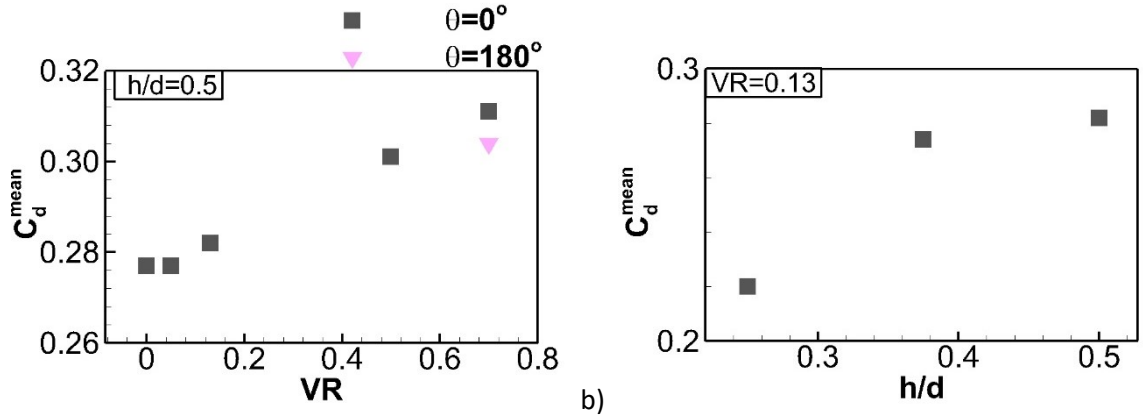

Fig. 16 Mean streamwise drag coefficient, C_d^{mean}. a) C_d^{mean} vs. VR= U_e/U_o for h/d=0.5; b) C_d^{mean}vs. h/d for VR=0.13.

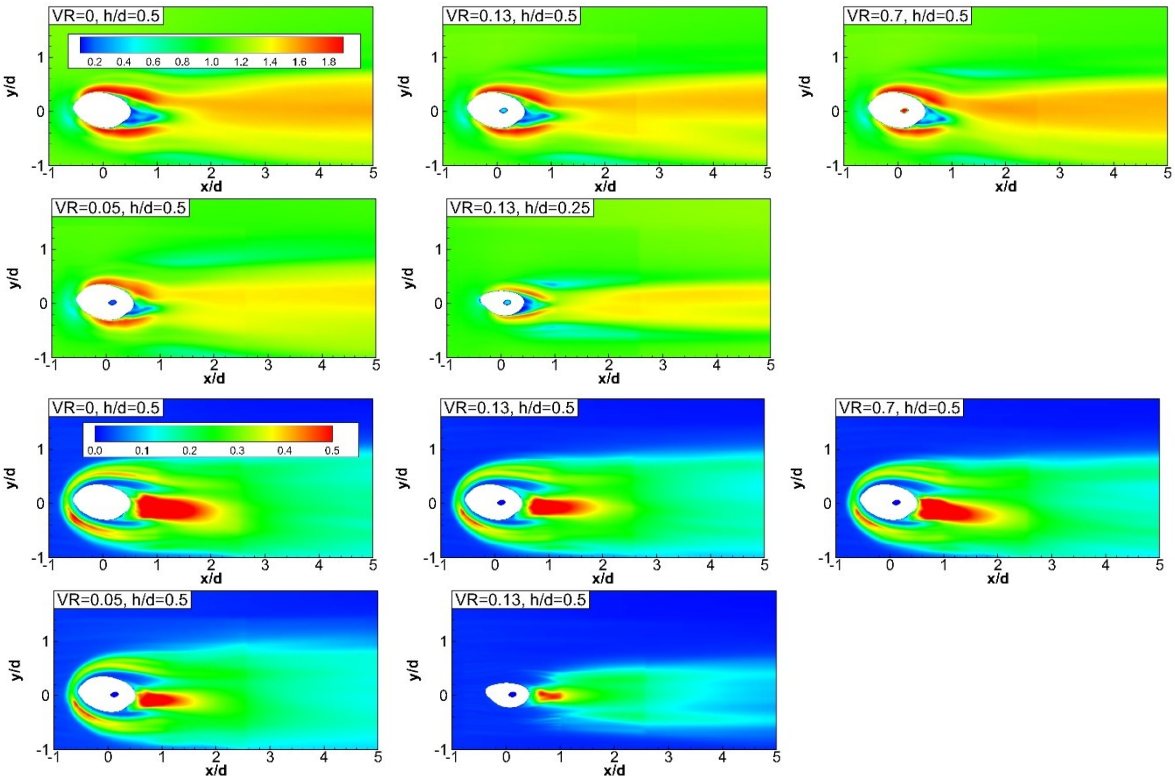

Fig. 17 Bed shear stress (θ=0^0 cases). a) mean bed shear stress magnitude, $\overline{\tau}/\overline{\tau}_0$; b) rms of the bed shear stress fluctuations, $\tau_{rms}/\overline{\tau}_0$.

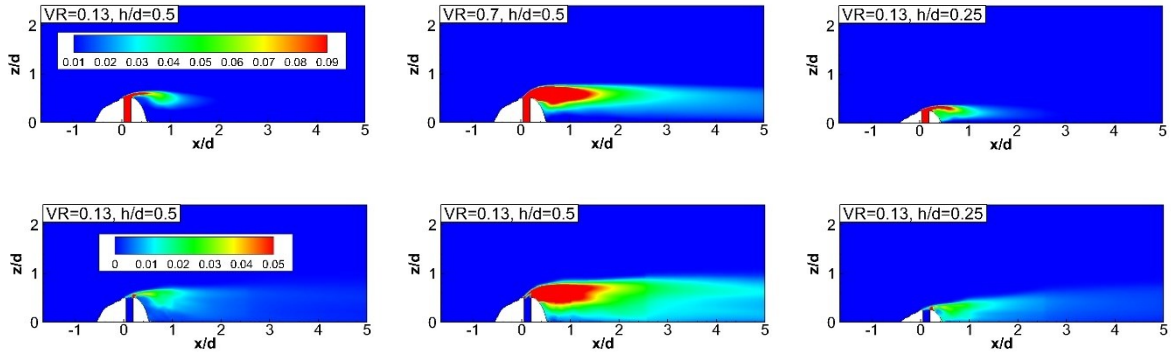

a)

b)

Fig. 18 Transport of passive scalar introduced in the excurrent siphon ($\theta=0^0$ cases). a) Mean concentration, C/C_0; b) rms of the concentration fluctuations, C'/C_0. The distributions are shown in the y/d=0 plane.

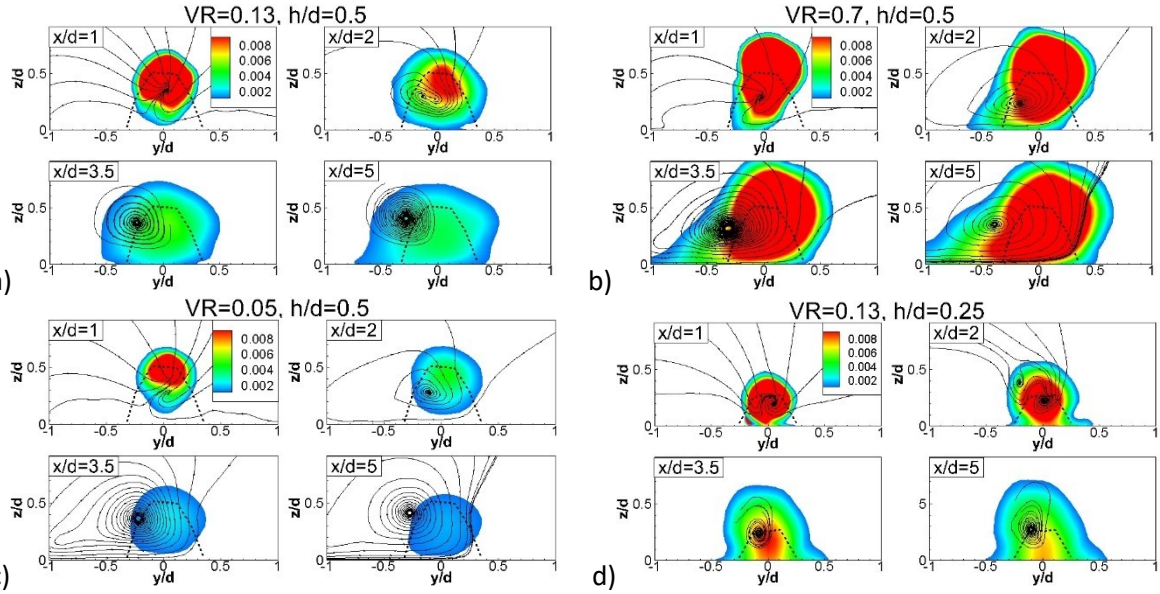

a)

b)

c)

d)

Fig. 19 Mean concentration of the passive scalar introduced in the excurrent siphon, C/C_0, in several x/d=constant planes ($\theta=0^0$ cases). a) VR=0.13, h/d=0.5; b) VR=0.7, h/d=0.5; c) VR=0.05, h/d=0.5; d) VR=0.13, h/d=0.25. The dotted line shows the projection of the mussel's shell. Also shown are the mean flow, 2-D streamline patterns.

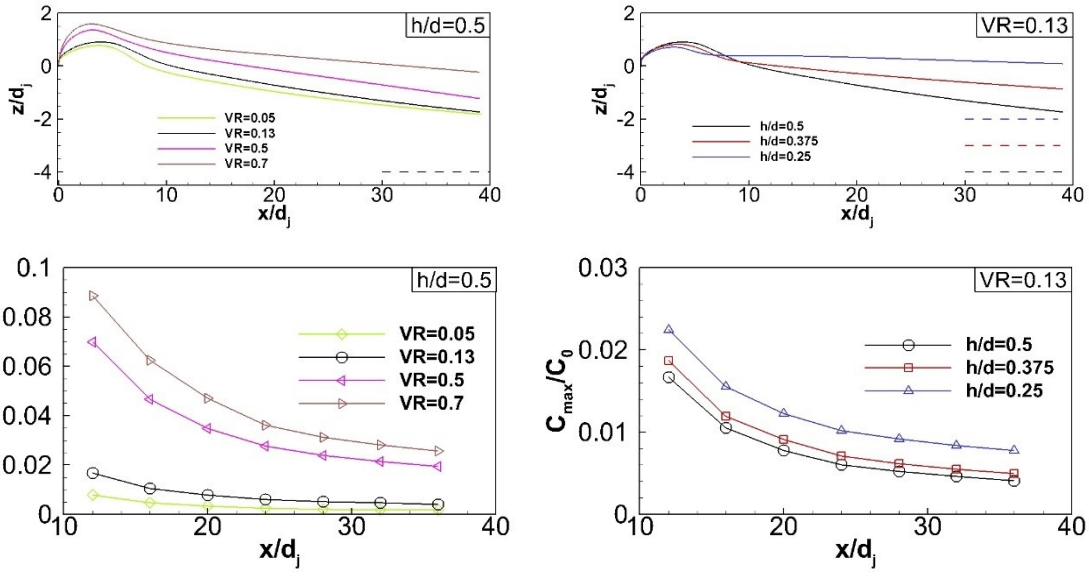

a)

b)

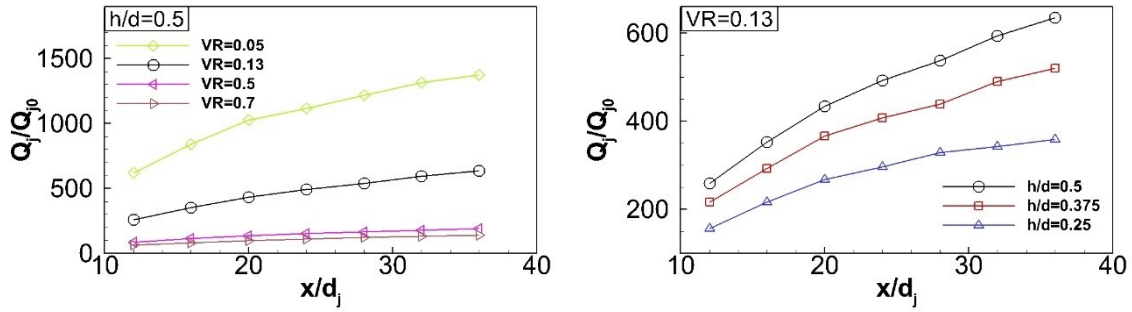

c)

Fig. 20 Characterization of the excurent siphon jet ($\theta=0^0$ cases). a) Centerline trajectory in the y/d=0 plane; b) Nondimensional peak scalar concentration, C_{max}/C_0; c) Nondimensional volume flux, Q_j/Q_{j0}.